

TOWARDS SILICON BASED LIGHT EMITTING DEVICES:  
PHOTOLUMINESCENCE FROM TERBIUM DOPED SILICON  
MATRICES WITH OR WITHOUT NANOCRYSTALS

A THESIS SUBMITTED TO  
THE GRADUATE SCHOOL OF NATURAL AND APPLIED SCIENCES  
OF  
MIDDLE EAST TECHNICAL UNIVERSITY

BY

BUKET KALELİ

IN PARTIAL FULFILLMENT OF THE REQUIREMENTS  
FOR  
THE DEGREE OF MASTER OF SCIENCE  
IN  
PHYSICS

JUNE 2009

Approval of the thesis:

**TOWARDS SILICON BASED LIGHT EMITTING DEVICES:  
PHOTOLUMINESCENCE FROM TERBIUM DOPED SILICON  
MATRICES WITH OR WITHOUT NANOCRYSTALS**

submitted by **BUKET KALELİ** in partial fulfillment of the requirements for the degree of **Master of Science in Physics Department, Middle East Technical University** by,

Prof. Dr. Canan Özgen  
Dean, Graduate School of **Natural and Applied Sciences** \_\_\_\_\_

Prof. Dr. Sinan Bilikmen  
Head of Department, **Physics** \_\_\_\_\_

Prof. Dr. Raşit Turan  
Supervisor, **Physics Dept., METU** \_\_\_\_\_

Dr. Ercan Yılmaz  
Co-Supervisor, **Physics Dept., Abant İzzet Baysal Univ.** \_\_\_\_\_

**Examining Committee Members:**

Prof. Dr. Atilla Aydınlı  
Physics Dept., Bilkent University \_\_\_\_\_

Prof. Dr. Raşit Turan  
Physics Dept., METU \_\_\_\_\_

Prof. Dr. Mehmet Parlak  
Physics Dept., METU \_\_\_\_\_

Dr. Hakan Altan  
Physics Dept., METU \_\_\_\_\_

Dr. Ercan Yılmaz  
Physics Dept., Abant İzzet Baysal Univ. \_\_\_\_\_

**Date:** \_\_\_\_\_ 17.06.2009 \_\_\_\_\_

**I hereby declare that all information in this document has been obtained and presented in accordance with academic rules and ethical conduct. I also declare that, as required by these rules and conduct, I have fully cited and referenced all material and results that are not original to this work.**

Name, Last name : BUKET KALELİ

Signature :

# ABSTRACT

## TOWARDS SILICON BASED LIGHT EMITTING DEVICES: PHOTOLUMINESCENCE FROM TERBIUM DOPED SILICON MATRICES WITH OR WITHOUT NANOCRYSTALS

Kaleli, Buket

M.Sc., Department of Physics

Supervisor : Prof. Dr. Raşit Turan

Co-Supervisor: Dr. Ercan Yılmaz

June 2009, 75 pages

In this study, silicon (Si) rich silicon dioxide (SiO<sub>2</sub>) films and terbium (Tb) embedded in three different Si containing films has been produced by e-beam evaporation and magnetron sputtering techniques. Post deposition annealing was done for different temperatures and durations to study its effect on both Si nanocrystal formation and Tb luminescence. It was verified by X-ray diffraction technique (XRD) that Si nanocrystals were formed in Si rich matrices. Energy dispersive X-ray (EDS) spectroscopy analysis was carried out to determine the relative concentrations of the atoms inside the produced films. X-ray photoelectron spectroscopy (XPS) gave the evidence of different bonding structures inside the Tb-Si-O containing films. Depth profile measurements were carried out to analyze changes in the relative concentration during sputtering of the layers after annealing of the Tb containing film. Luminescence characteristics of Si nanocrystals and Tb<sup>3+</sup> ions were studied by photoluminescence (PL)

spectroscopy. It was observed that  $Tb^{3+}$  luminescence enhanced by an energy transfer from Si nanocrystals and trap levels in a matrix. This result supplies valuable information about the excitation paths of  $Tb^{3+}$  ion the way of intense luminescence.

Keywords: Magnetron Sputtering, Si nanocrystals, Terbium, Photoluminescence Spectroscopy.

# ÖZ

## SİLİSYUM IŞIK YAYAN DİYOTLARA DOĞRU: TERBİYUM İLE KATKILANMIŞ NANOKRİSTAL İÇEREN VEYA İÇERMEYEN SİLİSYUM MATRİSLERİN FOTOLÜMİNESANSI

Kaleli, Buket

Yüksek Lisans, Fizik Bölümü

Tez Yöneticisi : Prof. Dr. Raşit Turan

Ortak Tez Yöneticisi: Dr. Ercan Yılmaz

Haziran 2009, 75 sayfa

Bu çalışmada Si açısından zengin SiO<sub>2</sub> filmler ve terbiyum (Tb) ile katkılanmış Si içeren üç farklı film elektron ışını buharlaştırması ve mıknatıslı saçtırma yöntemleriyle üretilmişlerdir. Değişik sıcaklıkların Si nanokristal ve terbiyum ışımaya etkisini incelemek için filmler üretim sonrası farklı sıcaklıklarda ve sürelerde fırınlamaya tabi tutulmuşlardır. X-ışını kırınımı (XRD) tekniği sonuçlarına göre Si nanokristallerin oluştuğu belirlenmiştir. Enerji dağılım X-ray (EDS) analizi filmlerin içerisindeki atomik konsantrasyon miktarlarını belirlemek amacıyla kullanılmıştır. X-ışını fotoelektron spektroskopisi (XPS) Tb-Si-O arasındaki farklı bağ oluşumları hakkında fikir vermiştir. Derinlik profili analizi fırınlamadan sonra değişebilecek olan her tabakadaki atomik konsantrasyonları incelemek amacıyla yapılmıştır. Si nanokristallerin ve Tb<sup>3+</sup> iyonlarının ışımaya özellikleri fotoluminesans (PL) yöntemi ile incelenmiştir. Elde edilen verilere göre Tb<sup>3+</sup> ışımaya matrisdeki Si nanokristallerden ve tuzak seviyelerinden enerji

transferi sayesinde artmaktadır. Bu sonuç  $Tb^{3+}$  iyonunun uyarılma mekanizmaları hakkında bilgi verici niteliktedir.

Anahtar Kelimeler: Miknatıslı Saçtırma, Si nanokristaller, Terbiyum, Fotolüminesans Spektroskopisi.

*to my lovely family...*

## ACKNOWLEDGEMENTS

I would like to thank to my supervisor Prof. Dr. Raşit Turan, for his perceptiveness, encouragement and being not only the supervisor but also the good friend of all of us. Without his guidance in my work, nothing would be that comfortable.

I want to thank to my present and former group partners Arife Gencer, Ayşe Seyhan, Seda Bilgi, Umut Bostancı, Nader A. P. Moghaddam, Selçuk Yerci, Seçkin Öztürk, Urcan Güler, Sedat Canli, Z. Deniz Eygi Dr. Ercan Yılmaz and Döndü Şahin for their friendliness and endless support during this work. I really learned a lot from them about variety of things. My special thanks goes to Mustafa Kulakçı, although he sometimes make life unlivable place for me, for being a working partner of mine by sharing his invaluable comments and ideas about not only my thesis but also the life itself, to İlker Doğan for his support both experimentally and mentally during the whole period of my study, to İlker Yıldız for XPS measurements and to Yücel Eke for his technical support. I really appreciate to people in Central Laboratory for XPS, XRD and SEM measurements.

I would like to thank to Esin Akbaba, Aydan Yeltik, M. Meliz Metbulut, Selmin Ener for their great friendship, to Mübeccel Koyutürk and Fatma Çetiner for being my best friends with their patience during my extending working hours, to ODTU Aikido Dojo for having spent invaluable moments all together and to Efe Kemaneci for causing me to earn different outlook to the life and for his endless support during my whole study.

I would like to thank to Scientific and Technical Research Council of Turkey (TUBITAK) for financial support during this study.

# TABLE OF CONTENTS

ABSTRACT .....	iv
ÖZ .....	vi
ACKNOWLEDGEMENTS .....	ix
TABLE OF CONTENTS.....	x
LIST OF TABLES .....	xii
LIST OF FIGURES .....	xiii
LIST OF ABBREVIATIONS .....	xvii
CHAPTERS	
1. INTRODUCTION.....	1
1.1 Historical Perspective .....	1
1.2 Motivation .....	2
2. SILICON IN SILICON DIOXIDE MATRIX.....	4
2.1 Properties of SiO <sub>2</sub> Matrix .....	5
2.2 Silicon Nanocrystals in SiO <sub>2</sub> .....	8
2.2.1 Formation of Nanocrystals.....	11
3. THEORY OF TERBIUM LUMINESCENCE IN A MATRIX.....	13
3.1 Atomic Energy Levels .....	14
3.2 Cross Relaxation Process.....	16
3.3 Terbium in Silicon Matrix.....	17
3.3.1 Excitation Mechanisms of Terbium in Silicon.....	17
3.4 Terbium in Silicon Dioxide Matrix.....	20
3.5 Terbium in Silicon Rich Silicon Dioxide Matrix.....	21



## LIST OF TABLES

### TABLES

Table 5.1	Properties of samples produced by e-beam evaporation technique .....	35
Table 6.1	Properties of the samples produced by sputtering technique...	44
Table 6.2	Elemental compositions of the samples.....	53

# LIST OF FIGURES

## FIGURES

Figure 2.1 Atomic structure of SiO <sub>2</sub> .....	6
Figure 2.2 Major optical absorption and luminescence bands of defect centers inside SiO <sub>2</sub> (top) and on the surface of SiO <sub>2</sub> (bottom).....	7
Figure 2.3 Quantum confinement increases the effective bandgap of a silicon nanocrystal (in SiO <sub>2</sub> matrix) which has a smaller diameter than exciton Bohr radius.....	9
Figure 2.4 The theoretical and the experimental values for bandgap of Si nanocrystal obtained from optical absorption (unfilled symbols) and luminescence (filled symbols). Dashed and continuous lines are calculated values of bandgap with and without excitonic correction .....	10
Figure 2.5 Si nanocrystal formation in a SiO <sub>2</sub> matrix and nanocrystal luminescence.....	11
Figure 3.1 Atomic energy levels and corresponding wavelengths of Tb <sup>3+</sup> ion .....	15
Figure 3.2 The schematic of cross relaxation process between two Tb <sup>3+</sup> ions .....	16
Figure 3.3 Temperature dependence of Tb <sup>3+</sup> ion PL intensity in porous GaP (solid line) Dashed line shows the best fit to the equation 3.7.....	20
Figure 3.4 Schematic diagram of excitation mechanism of Tb <sup>3+</sup> ion via exciton recombination in Si nanocrystal.....	22
Figure 3.5 PL of Er implanted Si nanocrystals at different Er doses.....	22

Figure 3.6 Schematic diagram of excitation mechanism of Tb <sup>3+</sup> ion via exciton recombination in a Tb-O related trap level inside the bandgap.....	23
Figure 4.1 The schematic of the sputtering system.....	25
Figure 4.2 The schematic of e-beam evaporation system .....	26
Figure 4.3 The process occurring by taking an XPS spectrum.....	28
Figure 4.4 The experimental setup of the X-Ray diffraction device.....	29
Figure 4.5 X-ray diffraction schematics by crystal plane.....	30
Figure 4.6 XRD device used in this work a) X-ray tube b) Shutter c) Cross beam optics d) Solar slit e) Sample holder f) Solar slit g) Attenuator h) Detector i) in plane unit.....	31
Figure 4.7 Schematic band diagrams for the PL processes in direct and indirect gap materials. The shaded states represent electrons and holes in the conduction and valence bands respectively by the absorption of photons with energy larger than the bandgap.....	32
Figure 4.8 Band diagram illustrating non-radiative recombination a) via a deep level, b) via an auger process (the energy is dissipated by the excitation of a free electron in the conduction band or hole in the valence band) and c) radiative recombination.....	34
Figure 5.1 Schematics of the produced samples.....	36
Figure 5.2 XRD spectrum of pure Tb.....	37
Figure 5.3 XRD spectra of the samples S1, S3 and S4.....	37
Figure 5.4 XRD peak fit around $2\Theta = 28.5^\circ$ region of S2.....	39
Figure 5.5 Room temperature PL spectrum of S1 excited by Nd-YAG laser.	40

Figure 5.6 Room temperature PL spectrum of S1 annealed at 1050°C under N <sub>2</sub> for 30min then 1050 °C under O <sub>2</sub> for 1h. This spectrum was taken using He-Cd laser operating at 325nm.....	41
Figure 5.7 PL spectrums of S2 (a,b) and S3 (c,d) annealed under vacuum (a,c) and N <sub>2</sub> (b,d) environments.....	42
Figure 6.1 Schematics of the sputtered samples. a,b and c represents Si7, Si8, Si9; d,e and f represents Tb1, Tb6, Tb8 respectively.....	45
Figure 6.2 XPS depth profile corresponding to the Si2p <sub>3/2</sub> state of Tb7 annealed at 1000°C for 30min.....	46
Figure 6.3 XPS depth profiles corresponding to a) O1s and b) C1s states of Tb7 annealed at 1000°C for 30min.....	47
Figure 6.4 XPS depth profile corresponding to the Tb3d <sub>5/2</sub> state of Tb7 annealed at 1000°C for 30min.....	48
Figure 6.5 The change of intensity of the peaks in each sputter cycle.....	49
Figure 6.6 Change of XPS peak position corresponding to a) Tb3d <sub>5/2</sub> , O1s b) C1s, Si2p <sub>3/2</sub> states of Tb7 annealed at 1000°C for 30min.....	50
Figure 6.7 XRD spectrum of samples Tb6, Tb7 and Tb8.....	51
Figure 6.8 Si (111) peak at 2θ =28.6° for sample Tb1 annealed under vacuum condition at 1000°C for 30min. This peak is known to be originated from Si nanocrystals inside a matrix.....	52
Figure 6.9 SEM photographs of the samples Tb6 (left) and Tb7 (right) annealed at 1000°C for 30min under vacuum condition.....	53
Figure 6.10 PL of Si7, Si8, and Si9 annealed at 1000°C for 3h under N <sub>2</sub> environment. Excitation source was 532nm Nd-YAG laser.....	54
Figure 6.11 PL spectrum of Tb1 annealed at different temperatures and durations .....	57

Figure 6.12 Room temperature PL of Tb1 annealed at 1000°C for 1h under N <sub>2</sub> environment excited by He-Cd and Nd-YAG laser.....	57
Figure 6.13 Room temperature PL spectrum of Tb1 annealed at 900°C and 1000°C for 1h under vacuum (10 <sup>-5</sup> Torr) environment.....	58
Figure 6.14 PL spectrum of Tb8 annealed under vacuum (10 <sup>-5</sup> Torr) environment at 900°C and 1000°C for 30min and 1h.....	60
Figure 6.15 Room temperature PL of Tb6 annealed at 1000°C for 30min under vacuum condition (10 <sup>-5</sup> Torr).....	61
Figure 6.16 Room temperature PL of Tb7-1 annealed at 1000°C for 30min under vacuum condition (10 <sup>-5</sup> Torr).....	61
Figure 6.17 Room temperature PL of Tb1 annealed at 1000°C for 1h under a) vacuum environment b) vacuum + O <sub>2</sub> environment. Excitation source was 325nm He-Cd laser.....	62
Figure 6.18 PL spectrum of Tb8 annealed under N <sub>2</sub> environment before and after C implantation at 800°C, 900°C, 1000°C for 30min.....	64
Figure 6.19 Temperature dependent PL spectrum of Tb6 after annealing under vacuum at 1000°C for 30min. a) for temperatures higher than 200K b) for temperatures lower than 150K.....	66
Figure 6.20 Temperature dependent PL spectrum of Tb2 after annealing under vacuum at 1000°C for 30min. a) at 300K b) for temperatures lower than 50K. Data taken between temperatures 300-50K was not included in PL spectrums to eliminate confusion due to the broad defect luminescence.....	67
Figure 6.21 Change of PL intensity of Tb6 and Tb2 with respect to change of temperature.....	67

## LIST OF ABBREVIATIONS

EDS	Energy Dispersive X-ray Spectroscopy
FWHM	Full-Width Half-Maximum
CMOS	Complementary Metal Oxide Semiconductor
NBOHC	Non-bridging Oxygen Hole Center
ODC	Oxygen Deficiency Center
LED	Light Emitting Diode
PL	Photoluminescence
RF	Radio Frequency
DC	Direct Current
IC	Integrated Circuit
SCCM	Standard Cubic Centimeters per Minute
SEM	Scanning Electron Microscopy
UHV	Ultra High Vacuum
XPS	X-ray Photoelectron Spectroscopy
XRD	X-ray Diffraction

# CHAPTER 1

## INTRODUCTION

### 1.1 Historical Perspective

Semiconductor technology began to develop as early as 1830. The first semiconductor device composed of lead sulfide was generated by F. Braun for the purpose of rectification of signals to be detected by radio receivers [1]. After the born of semiconductor device, many other electronic components were produced. It was not until 1959 that the components became integrated in an electronic circuit. Each component had its own function before that date. To create the circuit, these components have had to be wired together. Due to the inefficiency of packaging and human involved wiring of each component, new methods were sought to make circuits. Although the integrated circuits were developed with transistor, resistor, and capacitor elements, interconnection was still a problem until J. Hoerni and R. Noyce developed a new process, called planar technology, at Fairchild Semiconductor in 1959. This technology enables diffusion of layers into the Si wafer to make a transistor and allows metal interconnects to be evaporated on the surface. This development made commercial production of integrated circuits (ICs) possible. By the end of 1960s, 90% percent of all the components were ICs [1].

### 1.2 Motivation

After its born around 1960s, microelectronics has evolved incredibly. It is now a mature technology dominating every part of our lives. Nonetheless, this enormous

rate of increase in data transfer rate and amount drive silicon microelectronics to its fundamental limits making researchers to develop new ways to extend this limitation. Silicon photonics is such a technology that increases the data transfer rate by using photons instead of electrons. Various device geometries for silicon photonics have been proposed, including optical clock signal distribution, optical links between processors and direct interfacing with existing optical fibre systems for high speed fibre to the home communication [2]. To constitute these devices, developments have been done for their elements such as photodetectors, modulators and electrically pumped optical sources. Compatibility of these elements with Si based Complementary Metal Oxide Semiconductor (CMOS) circuits is an important issue. Current level of technology enables almost all of elements to be demonstrated in Si, except an efficient optical source. Therefore, demand is to produce Si light emitter by using different approaches such as rare earth (RE) doping of Si based matrices.

Luminescence from RE atoms has attracted interest due to increasing demand for optical sources and amplifiers working in the range of low loss fiber optic communication, 1.5-1.6 $\mu\text{m}$ . However, the technological importance of RE luminescence goes beyond the telecommunication applications. It has become important for displays, laser materials, data storage, radiation detection, and medical applications. In addition, rare earth metal silicides (REM's) were shown to be superior to other metals in certain aspects such as low formation temperature, high thermal stability and hardness, relatively low resistivity and high chemical activity. REM's are known to create lowest schottky barrier heights (0.3 to 0.4 eV) on n-type silicon which makes them a potential candidate for infrared detectors and ohmic contacts whereas almost the highest barrier height (0.7 eV) on p-type Si with application as Schottky diodes [3]. Furthermore, due to having low resistivity, they can be used in interconnection lines instead of poly-Si which has limited conductivity [4]. REM's also have potential use in field effect transistors. This makes oxidation of metal silicides of particular interest in semiconductor technology to utilize it as a gate electrode.

In spite of its promising features in optoelectronics field of research due to their characteristic sharp atomic luminescence, RE's are not effective emitters and useless in their pure form. Therefore, to exploit atomic transitions effectively, it is very crucial to embed RE into different environments depending on the practical application.

The primary focus point in this work is to clarify PL mechanisms of Si based matrices doped with RE atom, Terbium, with or without nanocrystals. In chapter 2, Si nanocrystal in silicon dioxide ( $\text{SiO}_2$ ) matrix is studied by taking care of attention to the role of oxide on emission properties. In chapter 3, terbium atom's properties are examined by considering the matrix effect. In chapter 4, description about production and characterization techniques that were used in this work are provided. Chapter 5 and 6 includes all the analysis done for this work with the results that were obtained. Finally, chapter 7 is devoted to conclusion.

## CHAPTER 2

### SILICON IN SILICON DIOXIDE MATRIX

Silicon has many unique properties that make it indispensable. It is very abundant in nature and has high crystal quality. Its oxide form is very stable and has good insulating quality which is needed for many applications. Due to its superior properties, silicon is the main element for the microelectronic technology today. At this stage, the trend is to increase the working speed and circuit capacity by producing smaller components (transistors, diodes) for ICs, which comes with cross talking and overheating problems. Therefore, optical interconnects are needed to handle large amount of data processing with a very high speed in a very small area. In today's optoelectronic technology, laser diodes made of III-IV alloys are commonly used to convert electric signal to light which can then be transferred through optical fibers. The main problem in this approach is the difficulty in the incorporation of III-IV alloys into silicon microelectronic circuit because of technological difficulties such as growth of defect free GaAs on Si substrate. For this reason, laser diodes must be separated from the circuit. But this affects the transport and the size of the circuitry. If silicon light emitter was available, integration between the circuit and light generator would be very easy and the resultant circuitry would be very effective.

It is well known that Si is not a good light emitter due to its indirect bandgap, meaning that the position of conduction band minimum and valance band maximum is not at the same  $k$  (wavevector) value. To obtain a transition between these two band edges, a momentum transfer to or from the electron is needed. This requirement results in less probable radiative transitions. Therefore, transforming Si to a good light emitting material has been a dream for the

scientists and engineer working in this field. Many attempts with different approaches have tried to generate light from Si. One of the most promising and most recent approaches was the Canham's work on porous silicon [5] which demonstrated that porous silicon can emit visible light at room temperature. After this pioneering study, nanocrystalline research began to attract much attention. There has been enormous number of work and publications on this topic in recent years. Si (or Ge) nanocrystals have been seen as controllable and tunable structures for the production of Si based light emitting diodes and lasers.

Nanocrystals need a host matrix to be useful in electro optical applications. A host matrix, which interacts with the nanocrystals at its interface, has a vital role in their optical characteristics. This chapter begins with a discussion on SiO<sub>2</sub> which is the most widely used matrix for Si nanocrystal production. Then, brief information about the Si nanocrystal formation and luminescence in SiO<sub>2</sub> will be given.

## **2.1 Properties of Silicon Dioxide Matrix**

SiO<sub>2</sub>, also known as silica, is hard and colorless material. It is very abundant in earth's crust. Drinking glasses, bottles, and windows are everyday use form of SiO<sub>2</sub>. Most importantly, because of its property of being excellent insulator with high chemical stability, it is widely used in microelectronics.

SiO<sub>2</sub> has several different crystalline polymorphic forms determined by the pressure, temperature and reaction dynamics. But the bonding of atoms in many of these forms is the same. It is a tetrahedron with silicon at the center and four oxygen atoms surrounding it. The tetrahedral O-Si-O angle is 109.18° and the distance between the Si-O is 0.16nm which is slightly smaller than the sum of the covalent radii of Si and O atoms (0.18nm) which means atoms are slightly penetrating each other. Each O atom is bonded with two Si atoms with an angle varying from 100° to 170° by a very small change of bonding energy. It is important that rotation of the Si-O-Si bond around an axis is nearly free and this

results in easiness of formation of amorphous structures [6]. Figure 2.1 shows the atomic structure of  $\text{SiO}_2$ .

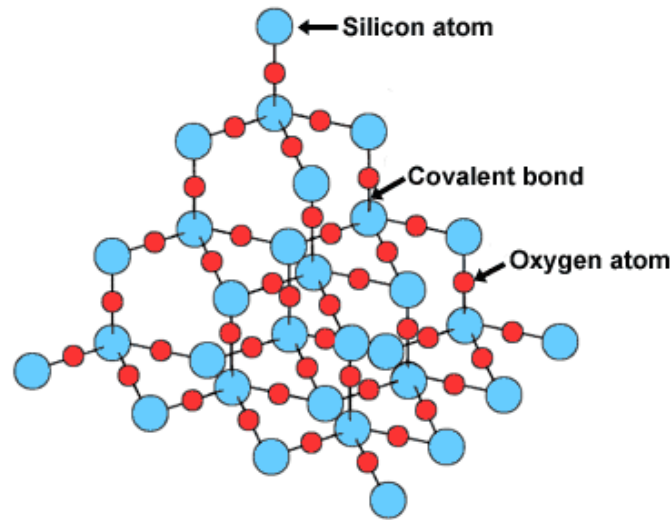


Figure 2.1: Atomic structure of  $\text{SiO}_2$  [7].

$\text{SiO}_2$  has several defects with different behaviors. When there is a transition between excited and ground states of the defects, emission peaks are generally broad. Oxygen deficient and oxygen excess centers are two most common defect centers which affects absorption and emission properties.

$E^{\cdot}$ -center is the mostly studied oxygen deficiency in silica. It occurs when hole is trapped in an oxygen vacancy. This center has 5.8 eV absorption band and 0.8 eV full width half maximum (FWHM). When there is a photo excitation into this band, no luminescence occurs. Although the nature of the electronic transition to this band has not been understood exactly, widely accepted idea is that it is caused by the charge transfer between the lower and upper Si atom. In that assumption, character and parameters of the absorption is highly depending on the nearest neighbor oxygen atom. Because of that reason property of  $E^{\cdot}$ -centers are different at the surface and inside the crystal [8]. Another oxygen deficient center is known as ODC has absorption band at 5 eV, singlet PL emission band at 4.4 eV and

triplet PL emission band at 2.7 eV (with 10.2ms decay constant). The predicted origin is known as the interaction of the positively charged Si with adjacent bridging oxygen.

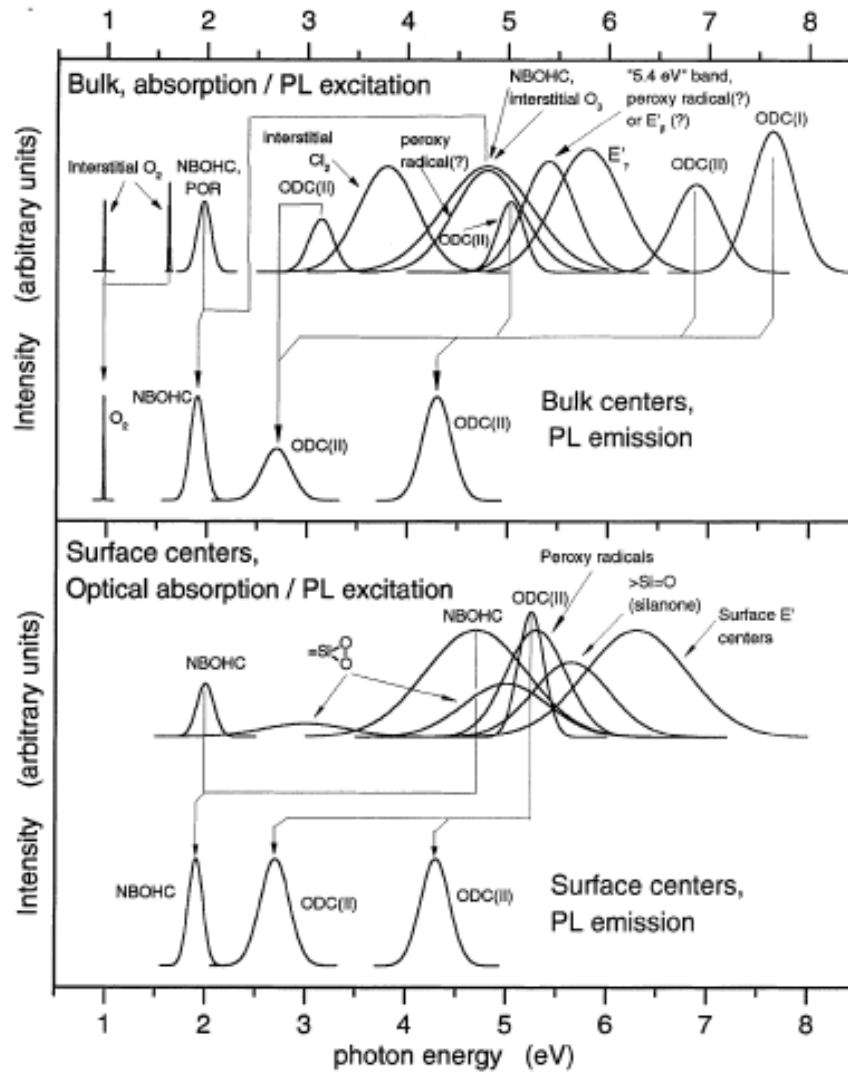


Figure 2.2: Major optical absorption and luminescence bands of defect centers inside SiO<sub>2</sub> (top) and on the surface of SiO<sub>2</sub> (bottom) [9].

Mostly known oxygen excess center defect is non-bridging oxygen hole center (NBOHC). This center occurs when Si-O bond is broken and creating an oxygen dangling bond. Its absorption band is at 4.8 eV with FWHM 1.07 eV. There is also an asymmetric absorption band at 1.97 eV with FWHM 0.17 eV and

photoluminescence band at 1.91 eV with FWHM 0.17 eV. These defects were detected and studied by many of the researchers up to now [10]. Figure 2.2 shows defect emission and absorption lines of silica mentioned above.

## 2.2 Silicon Nanocrystals in SiO<sub>2</sub>

The idea behind the properties of nanocrystallites comes from the quantum mechanics. Electron's free motion is quantized when it is trapped in a quantum dot and quantum confinement effects begin to occur. Quantum confinement can be described as a change in bulk properties when the size is shrinking. This effect occurs when one or more of the dimensions of a crystal are made very small so that it approaches the size of an exciton in bulk crystal, called the Bohr exciton radius and defined by,

$$a_b = \frac{4\pi\hbar^2\epsilon_r\epsilon_0}{\mu e^2} \quad (2.1)$$

where  $\mu$  is the reduced mass of the electron-hole pair,  $e$  is the charge of electron,  $\epsilon_r$  is the dielectric constant of the silicon and  $\hbar$  is the Planck's constant [11]. This value is 4.3 nm for bulk silicon.

The difference in properties of the bulk and confined systems is generally due to the difference between the density of states. For bulk materials density of states are proportional to  $E^{1/2}$  whereas in a quantum dot (0D structure) it has delta function type energy dependence. This means that for an ideal system energy levels are well separated from each other, but due to the interactions of quantum dots with host matrix and impurity atoms, broadening of energy levels occurs.

To explain the quantum confinement effect, effective mass approximation is used [11]. It suggests that electrons and holes in semiconductor are independent particles with an effective masses  $m_e^*$  and  $m_h^*$ . In this model, silicon nanocrystal is thought as a spherical potential well that bounds an exciton. Bandgap of the

nanocrystal can be described by the effective mass approximation with linear dimensions,  $L_x, L_y, L_z$  as [12]:

$$E_{gapnc} = E_{gapbulksi} + \frac{\hbar^2 \pi^2}{2} \left( \frac{1}{m_e^*} + \frac{1}{m_h^*} \right) \left( \frac{1}{L_x^2} + \frac{1}{L_y^2} + \frac{1}{L_z^2} \right) \quad (2.2)$$

where  $E_{gapbulksi} = 1.12 \text{ eV}$

In this expression it can be easily seen that energy necessary to generate electron-hole pair increases by decreasing the size of the system leading to a shift in the emission to shorter wavelengths. Figure 2.3 shows this effect schematically for 3nm Si nanocrystal in a  $\text{SiO}_2$  matrix.

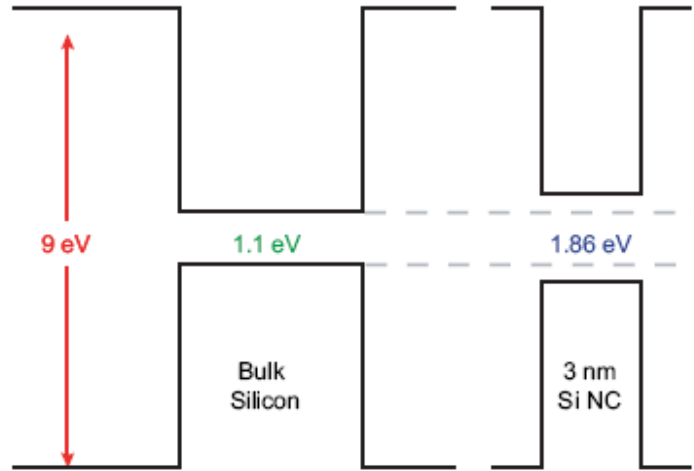


Figure 2.3: Quantum confinement increases the effective bandgap of a silicon nanocrystal (in  $\text{SiO}_2$  matrix) which has a smaller diameter than exciton Bohr radius [13].

Bandgap increase by decreasing nanocrystal size is also supported by theory and experiments. The following figure shows energy gap change of Si nanocrystal with respect to nanocrystal diameter.

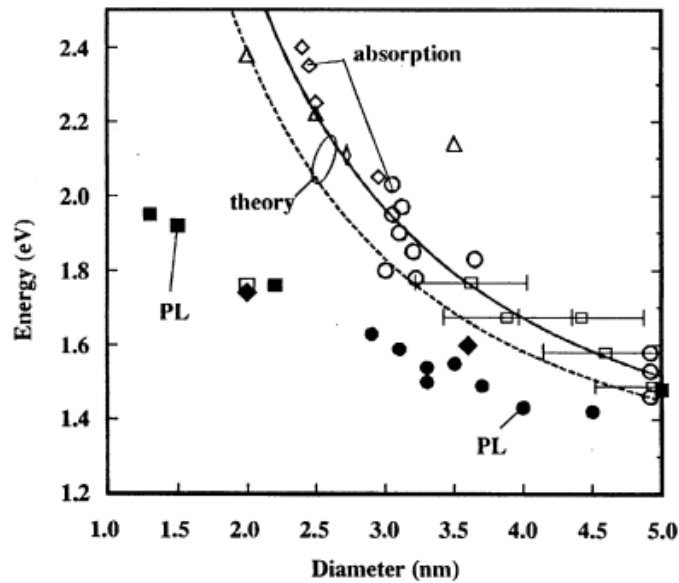


Figure 2.4: The theoretical and the experimental values for bandgap of Si nanocrystal obtained from optical absorption (unfilled symbols) and luminescence (filled symbols). Dashed and continuous lines are calculated values of bandgap with and without excitonic correction [14].

Both experiment and theory show that there is an increase in the band gap of the crystal and the exciton binding energy when cluster size decreases. Therefore, by changing the size of the nanocrystals, band to band emissions at different wavelengths can be achieved [15]. Another advantage of the confinement effect shows itself when crystal in its bulk form has an indirect band gap. To get emissions from indirect gap materials, phonons are need to be emitted or absorbed. Due to low probability of this process, indirect gap materials are generally inefficient light emitters. If electron and hole wave functions are confined in a quantum dot, their position will be better defined and this increases the uncertainty in crystal momentum  $k$  allowing optical transitions between bands without requiring phonon involvements. Hence, radiative transition rate of excitons are enhanced in a confined structures.

### 2.2.1 Formation of Nanocrystals

Mostly accepted mechanism for nanocrystal formation is the Ostwald ripening [16]. This is a thermodynamically driven spontaneous process. Larger particles has low surface to volume ratio, meaning lower surface energy. Since the system tries to minimize its energy, interfacial area has to decrease in time. To decrease the interfacial area, smaller particles gets much smaller while the larger particle gets much larger. Figure 2.5 shows the formation and luminescence of the nanocrystals.

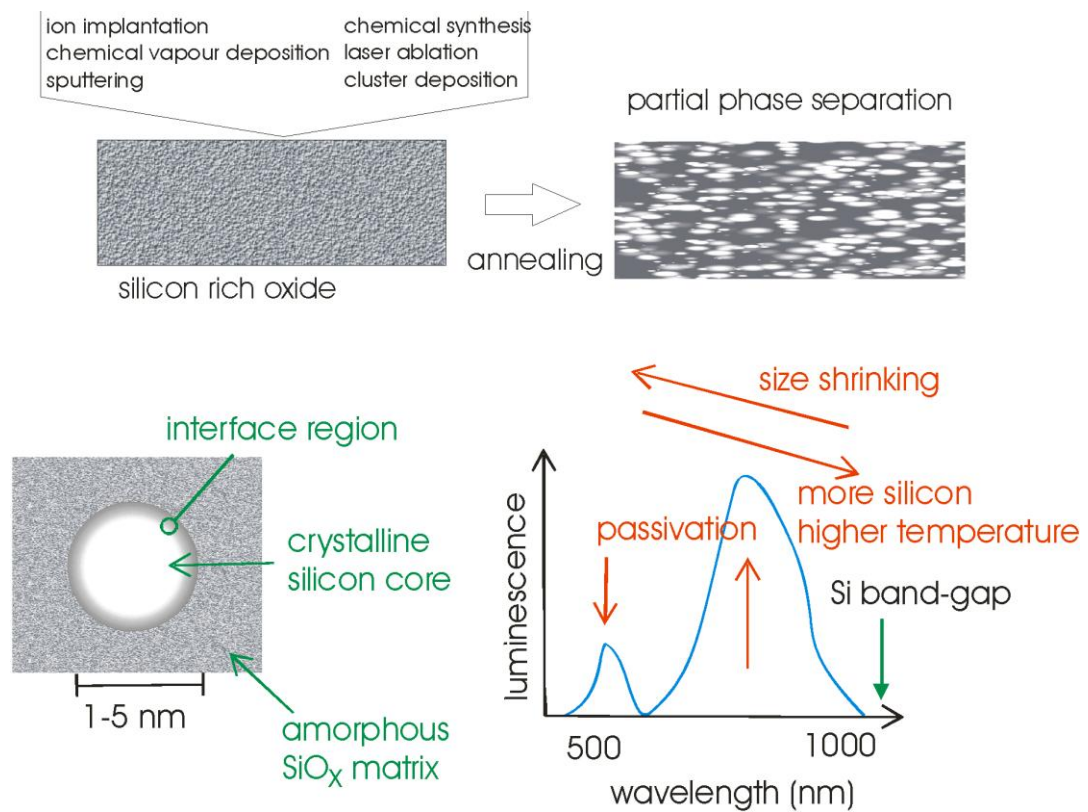


Figure 2.5: Si nanocrystal formation in a  $\text{SiO}_2$  matrix and nanocrystal luminescence [18].

$\text{Si}$  rich  $\text{SiO}_2$  is generally studied matrix to form  $\text{Si}$  nanocrystals. If  $\text{Si}$  concentration is higher than 2% in  $\text{SiO}_2$  matrix and the separation between the atoms is around 1nm, even without thermal treatment, phase separation can begin

to occur and small clusters formed. Annealing is needed to induce further growth of the nanostructures. Nanocrystal size achieved after annealing depends on concentration, annealing time and temperature. Due to small diffusion constant, formation of Si nanocrystals in SiO<sub>2</sub> requires high temperature treatment -above 900°C- for long durations [17].

## CHAPTER 3

# THEORY OF TERBIUM LUMINESCENCE IN A MATRIX

*These elements [rare earths] perplex us in our researches, baffle us in our speculations and haunt us in our dreams. They stretch like an unknown sea before us-mocking, mystifying, and murmuring strange revelations and possibilities.*

Sir William Crookes (1887)

Recently, several different approaches have been reported to achieve light from silicon based devices. One of the promising approaches is to dope a Si based matrix with a RE element. Erbium (Er) as a RE element has attracted much more attention because of the well known  $\text{Er}^{3+}$  4f-intrashell transition at 1.54  $\mu\text{m}$  which is applicable to telecommunication. For this important application researchers have studied Er luminescence in details. Although Er is mostly studied dopant, there are also studies with other rare earth elements such as Terbium (Tb), Ytterbium (Yb) and Gadolinium (Gd) having emissions at 543 nm, 980 nm and 316 nm respectively [19-23]. Even though PL properties of  $\text{SiO}_2$ : RE materials have been studied extensively, the emission mechanism is still controversy and efficiency achieved is very low when compared with commonly used III-V compounds. In addition, EL properties of these materials have not been studied deeply because of the poor injection of carriers into the  $\text{SiO}_2$  layer and poor reliability at high biases.

To solve the problems encountered in PL and EL application, several approaches have been made. Firstly it has been attempted embedding RE into silicon matrix. But the efficiency was too low at room temperature due to the back transfer

process. Then, they were embedded in SiO<sub>2</sub> layer of Si MOS device and by this approach high efficiencies were reported. But the reliability of these devices is limited by the charge to breakdown and the threshold voltage. In the last approach, RE ions and nanocrystals are both introduced into SiO<sub>2</sub>. These films show improved stability at high bias but efficiency has reduced due to the created conducting pathways into dielectric matrix. In this latest approach the main mechanism of emission is that Si nanocrystal provides the energy which is transferred to the RE ion enabling it to have luminescence [19].

In this thesis, Tb was used as a RE dopant. It is one of the most abundant RE metal around the earth. It is used as dopant for many devices and as green phosphor for fluorescent lamps and TV screens. Due to being hard to be purified, only by a special technique called ion exchange, its cost is currently very high, making its applications limited. However, high cost can be compensated by high added value to today's micro and optoelectronic industry. Before presenting the results of this investigation, it is important to understand the fundamental properties of Tb.

### 3.1 Atomic Energy Levels

Having atomic number 65, Tb atom has an electronic configuration [Xe] 4f<sup>9</sup>6s<sup>2</sup>. In a matrix, it became ionized and electronic configuration of the Tb<sup>3+</sup> ions became [Xe] 4f<sup>8</sup>. Because of the unfilled 4f shell, although it is not the outermost shell, electrons in that shell are optically active. Outermost and filled 5s and 5p shells shield the optically active electrons from the environment, improving the luminescent properties.

Intra-4f transitions are forbidden in RE ions. But in a host crystal, dipole selection rules are relaxed and these transitions became partially allowed. The following figure shows the energy level diagram for Tb<sup>3+</sup> ion. It is called Dieke diagram [24], calculated for LaCl<sub>3</sub> host matrix. Due to the weak interaction between the host and the optically active electrons because of the shielding, this diagram is used to identify possible transitions in other matrices.

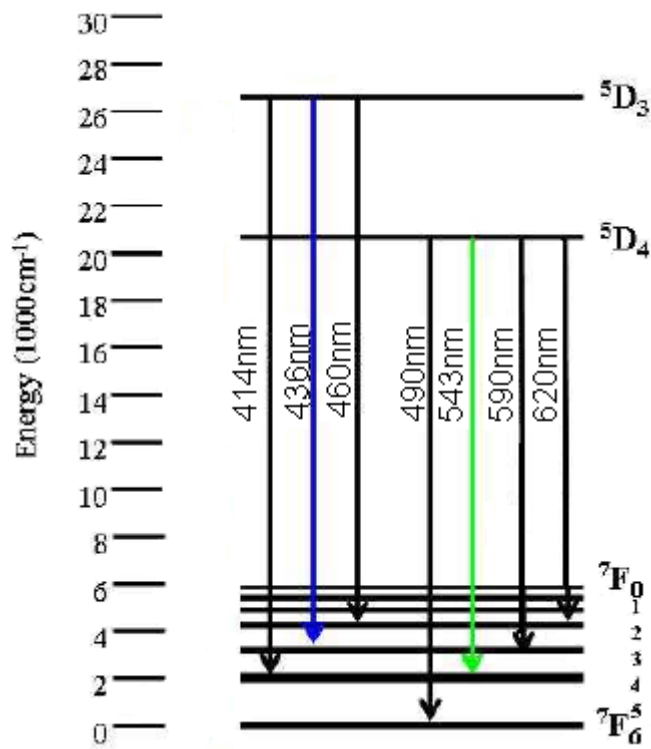


Figure 3.1: Atomic energy levels and corresponding wavelengths of Tb<sup>3+</sup> ion [25].

Although atomic transitions are generally give sharp peaks, there can be broadening due to the Stark splitting. This is because of the crystal field of the host matrix of Tb<sup>3+</sup> ion. At temperatures nearer to the room temperature stark splitting became the dominant reason for the broadening. But shielding of the 4f level makes spin-orbit coupling much dominant then the stark splitting [2].

Ion-ion interactions occur for Tb like other rare earths. Coulombic interaction between nearby ions can transfer energy from the excited ion to the one in the ground state (energy migration), between two excited ions to leave one in the ground state and the other in a higher energy state (co-operative upconversion) or from an ion in the high energy state to the other in the ground state leaving both in an excited state (cross relaxation). These interactions are due to dipole-dipole interactions depending on the distance between ions. Therefore, ion concentration is an important parameter effecting luminescence properties. If ions became aggregated, luminescence lifetime and efficiency can be reduced.

Among the all energy transfer interactions discussed above, cross relaxation process is a mostly observed interaction between two neighboring  $Tb^{3+}$  ions.

### 3.2 Cross Relaxation Process

In this process excited ion transfer its energy to the unexcited ion by a no-photon process. Finally both ions became excited. In rare earths generally due to the dipole-dipole interactions electric field coupling occurs and this result in cross relaxation process. Electric field is depending on the distance causing this process to depend on the distance between the ions. The following figure shows the cross relaxation process between two  $Tb^{3+}$  ions.

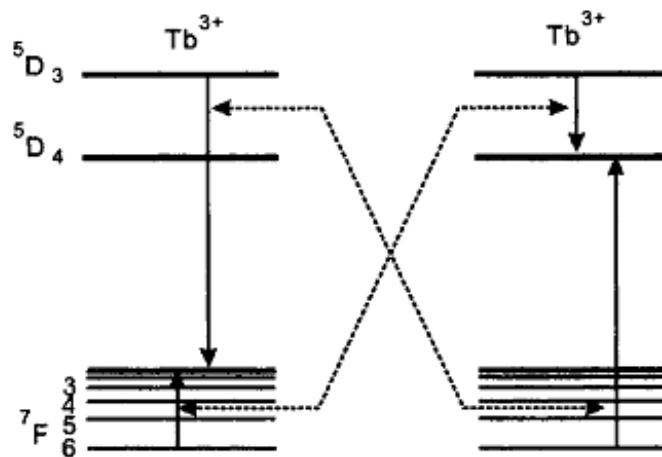


Figure 3.2: The schematic of cross relaxation process between two  $Tb^{3+}$  ions [21].

Cross relaxation process is likely occurring for  $Tb^{3+}$  ions in a silicon matrix [26]. When charges excited to  $^5D_3$  level, due to the small relaxation time, carriers are immediately transferred to another level either radiatively or non-radiatively. Therefore, in luminescence spectrum transition from  $^5D_3$  level to the  $^7F_j$  ( $j=1-6$ ) levels may not be seen. Studies about  $Tb^{3+}$  ion luminescence show that, emission from the  $^5D_3$  state can be seen when Tb concentration is around 0.05% and it disappears when Tb concentration exceeds 0.5% [20, 21] because of the higher possibility of cross relaxation between two  $Tb^{3+}$  ions, dominating the carrier

concentration in  $^5D_4$  level. In that case, only emissions because of the transitions from  $^5D_4$  level to  $^7F_j$  levels are observed.

### **3.3 Terbium in Silicon Matrix**

RE doped porous semiconductors takes much interest due to high incorporation of RE atoms into the matrix and easy charge injection. In addition, PL quenching due to high temperature is lower than the bulk host case because of the possible band gap increase. It is known that d-electrons of the transition metals are located in energy gap of semiconductors and threefold ionized free RE ion's 4f levels are separated from 5d levels by an energy gap larger than 20 eV [27]. The interaction with the host matrix produces splitting of the f-multiplets of the RE ions, relaxing the selection rules for dipole allowed transitions. Tb atom has a splitting of 4f multiplets about 1 eV while splitting due to the interaction with the matrix is much smaller. With the help of that information, one can imagine 4f levels below the valance band of the semiconductors [28]. These energy level alignments are slightly changed depending on the matrix of the ion by affecting excitation mechanisms. To understand the luminescence mechanism exactly, it is important to study on excitation of  $Tb^{3+}$  ion in a matrix studied.

#### **3.3.1 Excitation Mechanisms of Terbium in Silicon**

When rare earths are used as a dopant in semiconductors, they produce light emission centers. Due to the difference between bonding structure and atomic radii of the  $Tb^{3+}$  ion and silicon, occupying interstitial sites are more stable for  $Tb^{3+}$  ion than the substitutional sites.

Optical excitation is needed to occur inside the matrix to achieve RE ion luminescence. This process for  $Tb^{3+}$  ion can occur inside a matrix via two processes: direct photon absorption or carrier mediated excitation. Due to the higher absorption coefficient of Si than  $Tb^{3+}$  ion in the excitation range, former process is less likely to occur in Si matrix. Although, as mentioned above, 4f

levels has to be positioned below the valance band of Si,  $Tb^{3+}$  ion can also have trap levels like  $Er^{3+}$  ion in a Si matrix [29]. One of the widely accepted excitation mechanism is that excitation is possible when exciton recombination occurs in a trap state produced by RE ion and energy released from that state causes an auger process exciting  $Tb^{3+}$  ion . RE generated trap level was confirmed theoretically [30] and it was shown experimentally for  $Er^{3+}$  ion that they are donor levels [31]. Excitation generally occurs by exciton recombination trapped by this level. Being similar RE atom,  $Tb^{3+}$  ion can also be excited by a similar mechanism as  $Er^{3+}$  ion. However, electron trapped by this level can be excited to the conduction band thermally reducing excitation probability. To understand the quenching of PL intensity, let's formulate the intensity of emission for  $Tb^{3+}$  ion:

Intensity of the emission can be given as:

$$I \propto \frac{N_{Tb}^*}{\tau_{rad}} \quad (3.1)$$

where  $N_{Tb}^*$  is the concentration of excited  $Tb^{3+}$  ion and  $\tau_{rad}$  is the radiative lifetime. Assuming that almost every  $Tb^{3+}$  ion is in ground state, the concentration of the excited ions is given by [32]:

$$\frac{dN_{Tb}^*}{dt} = \frac{n_c}{\tau_{tr}} - \frac{N_{Tb}^*}{\tau} \quad (3.2)$$

Where  $n_c$  is the concentration of the  $e^-h$  complexes,  $\tau_{tr}$  is the time needed for energy transfer,  $\tau$  is the PL lifetime of  $Tb^{3+}$  ion. At steady state  $N_{Tb}^*$  is given by:

$$N_{Tb}^* = \frac{n_c \tau}{\tau_{tr}}, \quad (3.3)$$

Intensity is then given by:

$$I \propto \frac{n_c \tau}{\tau_{tr} \tau_{rad}} \quad (3.4)$$

To find the intensity, the concentration of the e<sup>-</sup>-h complexes needs to be formulated. The following relation will be used to extract  $n_c$ :

$$\frac{dn_c}{dt} = R_c - R_D - R_E \quad (3.5)$$

where  $R_c$  is the formation rate of the e<sup>-</sup>-h complexes and depend on the hole capture cross section, hole thermal velocity, hole concentration, occupation probability of the level by electron, Tb<sup>3+</sup> ion concentration that creates level in the bandgap;  $R_D$  is the dissociation rate of the complexes and depends on localized electron's emission rate to the conduction band and  $n_c$ ;  $R_E$  is the excitation rate of the ion by the mechanism proposed and given by  $n_c/\tau_{tr}$  [32].

If excitation rate  $R_E$  is taken as negligible,  $n_c$  can be written as:

$$n_c = N_{Tb}^* \left[ 1 + \frac{\sigma_n N_c}{\sigma_p G \tau_c} \exp\left(-\frac{E}{kT}\right) \right]^{-1} \quad (3.6)$$

Where  $\sigma_n$  and  $\sigma_p$  are the capture cross section for the electrons and holes,  $N_c$  is the effective density of states at the bottom of the conduction band,  $G$  is the optical generation rate of the e<sup>-</sup>-h pairs and  $\tau_c$  is the carrier lifetime.

Inserting the  $n_c$  relation to the intensity equation gives temperature dependent PL intensity relation for the Tb<sup>3+</sup> ion as:

$$I \propto N_{Tb}^* \frac{\tau}{\tau_{tr} \tau_{rad}} \left[ 1 + \frac{\sigma_n N_c}{\sigma_p G \tau_c} \exp\left(-\frac{E}{kT}\right) \right]^{-1} \quad (3.7)$$

this expression shows that due to the terms  $\tau$ ,  $\tau_{tr}$  and T, there is a temperature dependence on the intensity of the PL emission for the Tb<sup>3+</sup> ion.

Elhouichet et al. studied temperature effect on PL intensity for Tb<sup>3+</sup> ion in GaP and obtained good match between experiment and theory. Figure 3.3 shows the results obtained by assuming Tb<sup>3+</sup> ion creates trap level below the conduction band by 0.77 eV and taken  $\sigma_n N_c / \sigma_p G \tau_c$  as 8.5.

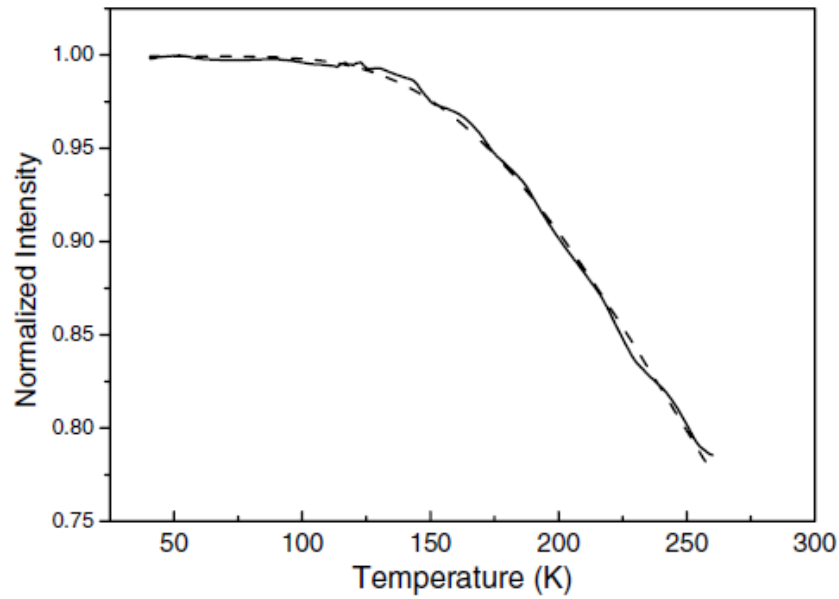


Figure 3.3: Temperature dependence of  $Tb^{3+}$  ion PL intensity in porous GaP (solid line). Dashed line shows the best fit to the equation 3.7 [32].

### 3.4 Terbium in $SiO_2$ Matrix

Silica is an important matrix because of its application in fibre technology. Recently, it has been used as a matrix to fabricate nanocrystal based Si light emitters. Oxygen containing matrix is thought to promote the RE optical activation by creating Tb-O defect levels [33]. Although oxygen atoms in the matrix may have an increasing effect on  $Tb^{3+}$  ion luminescence by creating Tb-O defect levels, it may indeed create shallower (if there are more oxygen bonded to the RE ion) or deeper (if there are less oxygen bonded to the RE ion) donor levels so that they cannot participate in the excitation of the RE ion. Therefore, it is believed that there is an optimum oxygen number bonding to the RE responsible for the luminescence [29]. Even though the relative concentrations of RE and O can be controlled by introducing much more RE atom inside the  $SiO_2$  matrix, due to decreasing effect of RE clusters in luminescence, intensity cannot be increased. Hence, it can be inferred that in  $SiO_2$  matrix there is generally much more than required O bonded with RE resulting shallower donor levels and decreases

luminescence. As a result, SiO<sub>2</sub> matrix is thought not to be suitable for achieving RE ion luminescence so that Si rich SiO<sub>2</sub> matrix is generally used instead.

### **3.5 Terbium in Silicon Rich Oxide Matrix**

Terbium in a Si rich SiO<sub>2</sub> matrix has been studied due to 3D confinement produced by SiO<sub>2</sub>-Si boundary and generation of Tb-O trap levels which then excite Tb<sup>3+</sup> ion. Si rich matrix is used to obtain nanocrystal based Si luminescence in many studies [17]. In these studies, Si size shrinks down to 2nm, it remains predominantly indirect bandgap and efficiency of the luminescence does not improve so much. However, recent studies shows that doping of Si nanocrystal containing matrix with a RE element may results in an effective luminescence. In this work, Si rich SiO<sub>2</sub> matrix was also studied and luminescence from Si nanocrystal was achieved. Addition of Tb into this system is the major focus point.

It has been reported that Si nanocrystals can transfer absorbed energy to the RE ion nearer to it resulting much intense luminescence in RE doped Si rich SiO<sub>2</sub> (figure 3.4). This process was studied for Er<sup>3+</sup> ion [12, 34] and it was shown that there is a competition between the RE ion and Si nanostructure luminescence as shown in figure 3.5. In this study, luminescence from the nanostructures was quenched when RE concentration increases. This behavior can be the direct evidence of energy transfer between nanocrystal and RE ion which enhances the emission. However, the mechanism is still controversy.

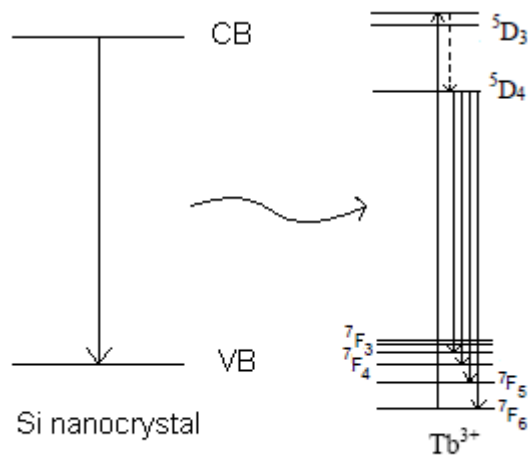


Figure 3.4: Schematic diagram of excitation mechanism of  $Tb^{3+}$  ion via exciton recombination in Si nanocrystal.

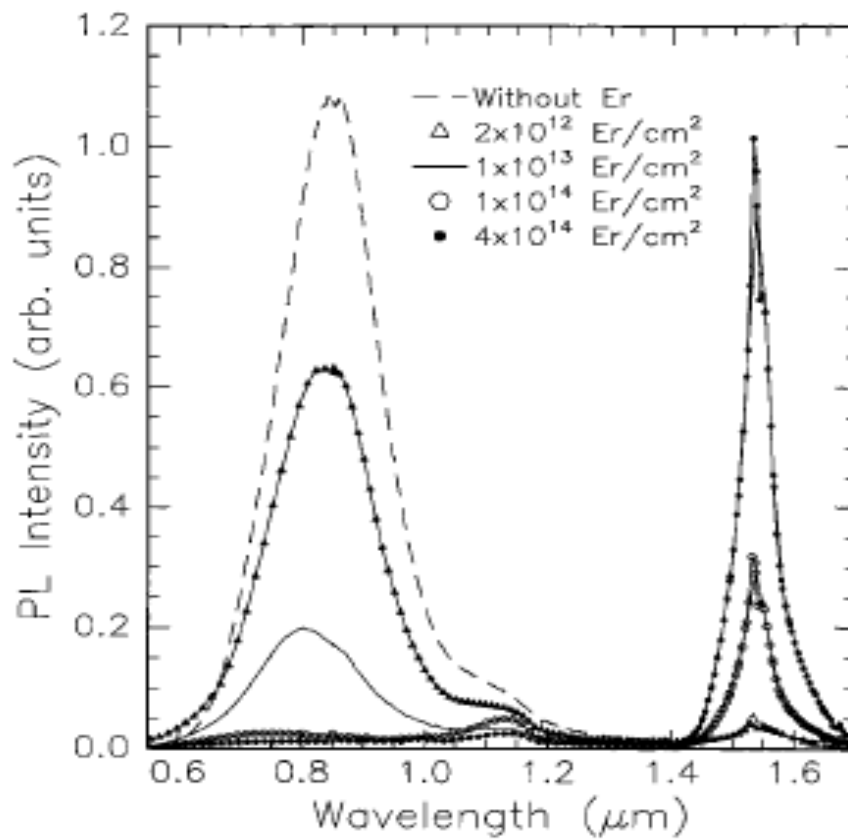


Figure 3.5: PL of  $Er^{3+}$  ion implanted Si nanocrystals at different Er doses [12].

The second property of this matrix is that its ability to generate Tb-O trap levels by limiting the oxygen bonded to Tb in an appropriate level so that created trap level position is suitable for excitation of  $Tb^{3+}$  ion. Figure 3.5 shows the possible excitation mechanism of  $Tb^{3+}$  ion by energy transfer from Tb-O related trap level inside the bandgap of the host matrix. The position of the Tb-O level in the bandgap is critical to induce a resonance with the  $Tb^{3+}$  ion atomic levels. The energy difference between the trap level and the level to which the electron makes transition should match the energy needed to excite the luminescent  $Tb^{3+}$  ion levels.

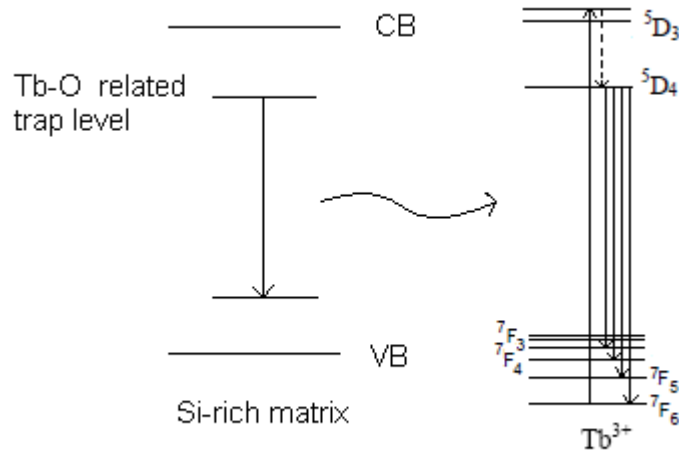


Figure 3.6: Schematic diagram of excitation mechanism of  $Tb^{3+}$  ion via exciton recombination in a Tb-O related trap level inside the bandgap.

## CHAPTER 4

# PRODUCTION AND CHARACTERIZATION TECHNIQUES

### 4.1 Magnetron Sputtering Deposition Technique

The magnetron sputtering deposition technique is based on the momentum transfer of ions to the target material. When atoms of the sputtering gas hits to the surface of the target, momentum transfer occurs by generating free atoms to be deposited on the substrate [35].

The process begins when gas atoms are entered to the high vacuum chamber. Due to being ionized while entering to the chamber, some of the gas atoms are attracted to the negatively charged target resulting in momentum transfer. Secondary electrons are generated by the further collisions between atoms. Excitation of the gas atoms by these electrons results in a plasma generation inside the chamber. In this technique magnetic field is used to confine the motion of the electrons generated by the collisions (Figure 4.1). Sputtering deposition is done after the medium get high vacuumed ( $1 \times 10^{-6}$  Torr). During deposition, gas pressure is set low to increase the rate. There are some other factors that affect the deposition rate in addition to the pressure of the chamber, such as mass of the sputtered atoms and energy of the gas particles [36].

There are several sputtering methods. But the most general ones are DC and RF sputtering techniques. While DC sputtering is very effective for the conducting targets, RF sputtering can be used to avoid the charging if non-conducting targets are needed to be sputtered.

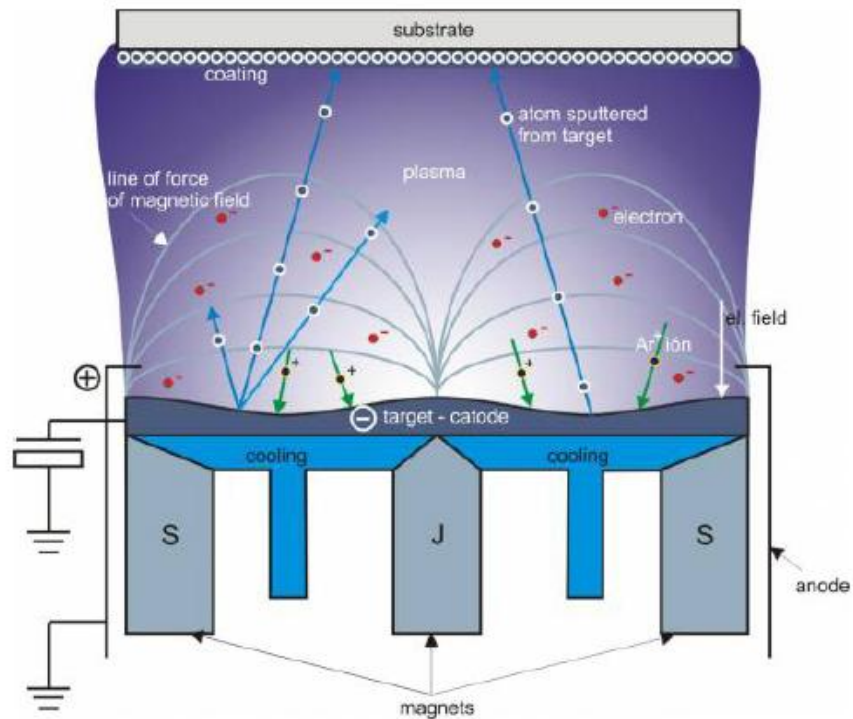


Figure 4.1: The schematic of the sputtering system [37].

#### 4.1.1 Experimental Setup

The sputtering set up used in this work is Nano D100 sputter deposition system which was produced by VAKSIS. It has 3 independently controlled magnetrons so that 2 DC and 1 RF sputtering can be done together. In this work, high purity argon gas was used as the sputtering gas. Gas flow and chamber pressure of the gas can be controlled electronically from a control panel. Power applied to the target is an important parameter for film growth by sputtering. In Nano D100 system, 13.56 MHz RF magnetron power can be increased up to 600W; while other two DC magnetron's power can be increased up to 500W and 1kW.

## 4.2 Electron Beam Evaporation Technique

In electron beam evaporation technique an energetic electron beam is focused on a source, making its temperature rise to above the value needed for evaporation. Evaporated target material is deposited on to the substrate as a thin film whose thickness is determined by the source parameters such as the beam current and the energy. This process takes place in a vacuum chamber to increase the mean free path and quality of the film. In this technique, there is a filament as the electron source and a magnetic field to focus electrons on the source. Magnetic field is needed because electrons are dispersed in a random manner when they are generated. Figure 4.2 shows our system schematically.

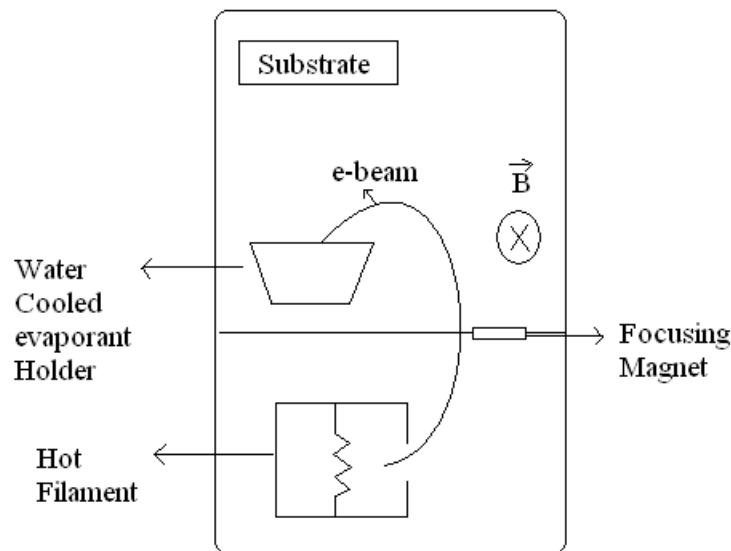


Figure 4.2: The schematic of e-beam evaporation system.

When electrons hit the source, their kinetic energy is transformed into thermal energy. The energy achieved by that technique is very high up to millions watt per square meter, Therefore, holder need to be water cooled to prevent melting.

### 4.3 X-Ray Photoelectron Spectroscopy

X-ray photoelectron spectroscopy (XPS) is a surface sensitive method in which X-ray beam is projected on the sample to eject electrons from core shell of the atoms. X-ray has to have energy greater than the sum of the binding energy of the electron and the work function of the material. The rest of the energy of an X-ray is spent as the kinetic energy of the electron which is analyzed to extract the binding energy of the material under investigation. Figure 4.3 shows the interaction of X-ray with an atom.

X-ray absorption is very fast, about  $10^{-16}$ s. Although X-ray penetrates about a micrometer depth, electrons ejected come from a thickness of about a few nanometers. Therefore, this method is very sensitive to the surface properties of the sample. In addition, chemical state of the surface elements, such as the oxidation of the surface atoms, can easily be determined by this method.

Since each element has characteristic set of core levels, kinetic energy of the emitted electrons can be used to differentiate the elements from each other [38] except hydrogen and helium due to having no inner shell electrons. This technique can also be used to determine relative concentrations of the elements if peaks can be analyzed correctly [39].

XPS analysis is done in ultra high vacuum conditions to increase the mean free path of the electrons ejected. XPS setup consists of X-ray source, hemispherical analyzer and detector. To make depth profile by this device, an ion gun can be included. XPS used in this thesis is a Specs Lab XPS system located at Central laboratory of METU. It uses Al K $\alpha$  line source with energy of 1486.6 eV. For depth profiling, 3500 eV Ar<sup>+</sup> ions were used to sputter the surface about an area of 3mm<sup>2</sup>.

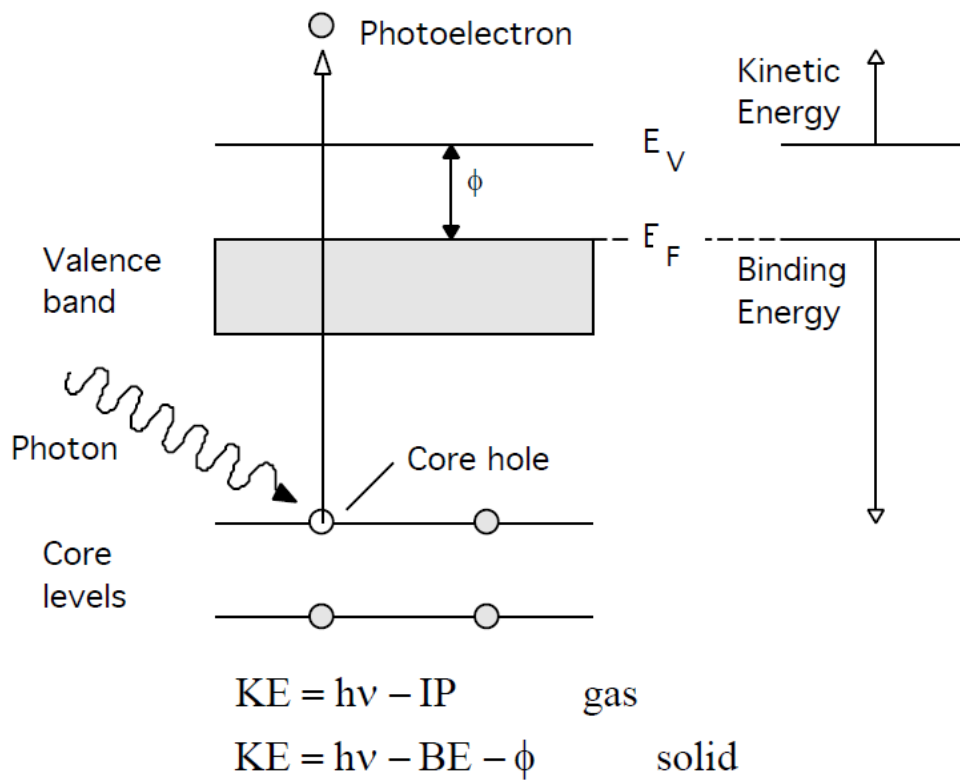


Figure 4.3: The process occurring by taking an XPS spectrum [38].

#### 4.4 X-Ray Diffraction

In this technique X-rays incident on a sample is scattered elastically by the electrons inside of the atoms. Scattered X-ray beam interfere destructively in almost all directions and in that case there is no energy released from the sample. But if atoms in a sample oriented in a regular pattern, constructive interference occurs in some directions and related peak can be observed by XRD.

X-Ray diffraction device has a simple structure with X-ray source, detector and movable sample stage. Figure 4.4 shows the experimental setup.

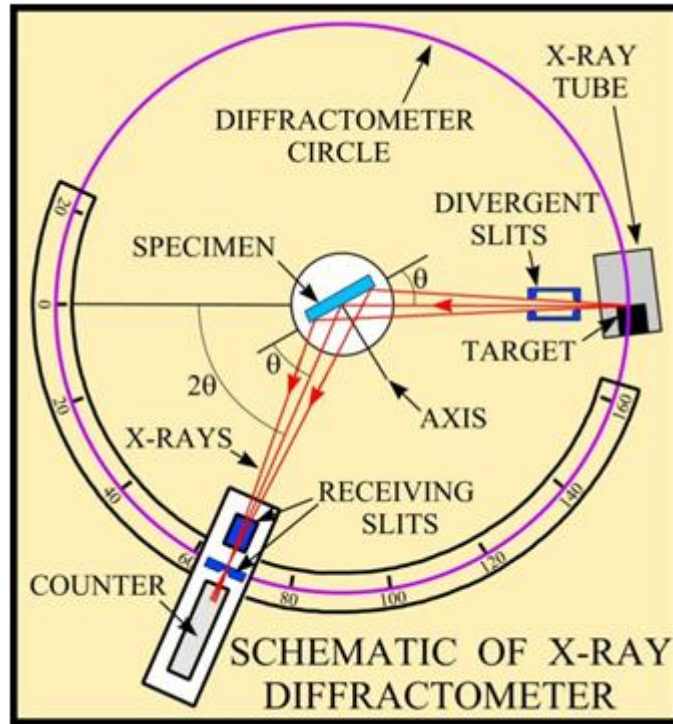


Figure 4.4: The experimental setup of the X-Ray diffraction device [40].

Theoretical study about the diffraction of an X-ray by the crystal lattice was done by W. G. Bragg. He stated the relation called Bragg's law given below.

$$n\lambda = 2d\sin\Theta \quad (4.1)$$

where  $n$  is the order of diffraction,  $\lambda$  is the wavelength of the X-Ray,  $\Theta$  is the angle of incidence and  $d$  is the spacing between the crystal planes, given by:

$$d = \frac{a_0}{\sqrt{h^2+k^2+l^2}} \quad (4.2)$$

Bragg's law is used to find the spacing between the crystal planes which is a fingerprint for every crystal. Figure 4.5 shows schematic of X-ray interaction with the crystal plane.

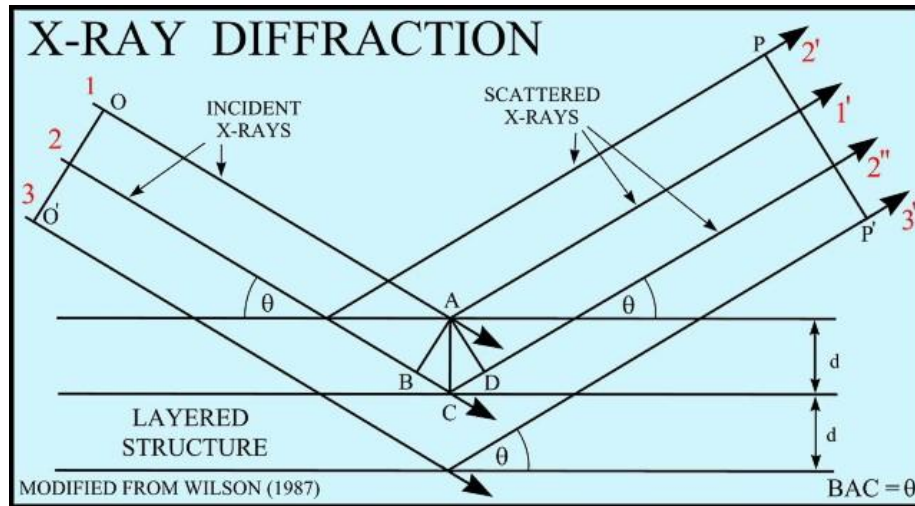


Figure 4.5: X-ray diffraction schematics by crystal plane [39].

During the scan of the angle of incidence, Bragg's law is satisfied at some  $\Theta$  values, a constructive interference occurs and a strong x-ray signal is detected by the detector. The output data is given by the intensity versus  $2\Theta$ , which is the angle between the incoming and the scattered beam.

In addition to analyzing different crystal orientations, X-ray diffraction data can also be used to find the mean size of the crystallites. This information is related to the broadening of the diffraction pattern and given by Scherrer's formula [41]:

$$D = \frac{K\lambda}{\beta \cos\theta} \quad (4.3)$$

Where  $\beta$  is the FWHM ( $I_{\max}/2$ ) of the diffraction peak,  $\lambda$  is the wavelength of the incoming X-ray,  $k$  is the Scherrer's constant depends on nanocrystal size and shape.

In this study XRD measurements were done by Rigaku Ultima-IV grazing angle XRD system situated in Central laboratory at METU with Cu  $K_{\alpha}$  40kV X-Ray source. Figure 4.6 shows the central part of the XRD equipment.

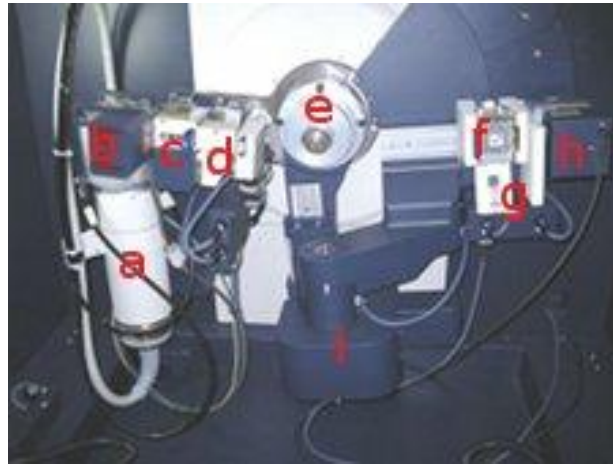


Figure 4.6: XRD device used in this work. a) X-ray tube b) Shutter c) Cross beam optics d) Solar slit e) Sample holder f) Solar slit g) Attenuator h) Detector i) In plane unit [42].

#### 4.5 Scanning Electron Microscopy

Scanning Electron Microscope (SEM) is a technique that uses electrons to analyze the surface features shape, size and composition. It has numerous advantages than optical microscopy that its magnification is 100 times that of optical microscope and its resolution can be down to 5nm.

When electrons hit the sample in a vacuum condition, large numbers of secondary particles are emitted such as secondary electrons, backscattered electrons auger electrons and X-rays. By collecting X-rays emitted from the sample, elemental composition and structure information can be achieved. Secondary electrons give surface feature information while backscattered electrons give compositional information about the sample. In SEM, secondary electrons and backscattered electrons are collected to form the magnified image of the surface topographies on the material. In addition, energy dispersive and wavelength dispersive detectors can be used with SEM for chemical analysis of the surface [43]. Detector collects energetic X-rays emitted from the sample. By collecting X-rays according to their energy, elemental peaks appear on the screen. Peak intensities give relative

amount of each element. If electron energy is increased, up to 10.000 keV, information from the deeper layer of the sample can be gathered.

In this work, a JEOL FEG SEM located in METU central laboratory was used with the energy dispersive detector [42].

#### 4.6 Photoluminescence Spectroscopy

Many of the materials can generate light when subjected to an excitation. In the photoluminescence technique, excitation source of materials are photons. The following figure shows the PL mechanism for direct gap and indirect gap materials.

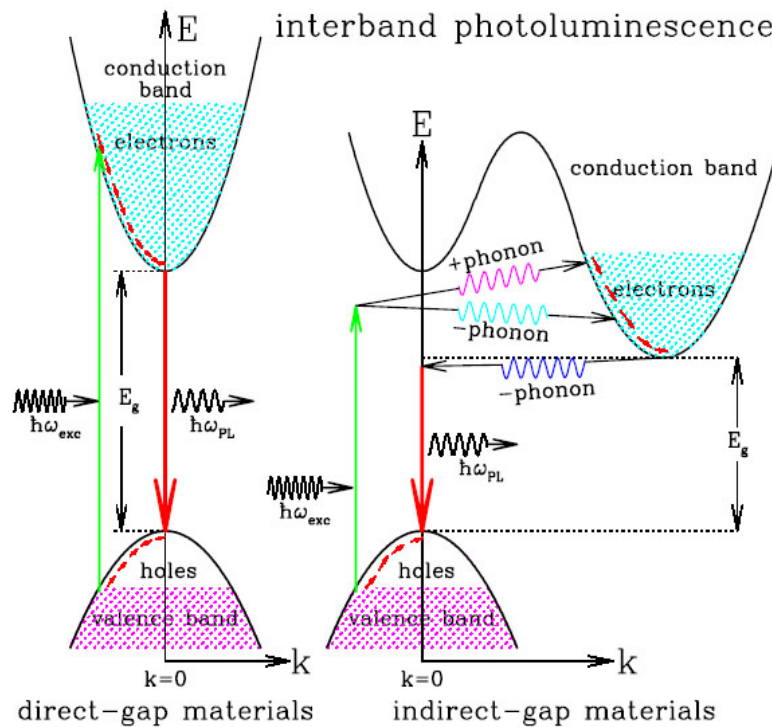


Figure 4.7: Schematic band diagrams for the PL processes in direct and indirect gap materials. The shaded states represent electrons and holes in the conduction and valance bands respectively by the absorption of photons with energy larger than the bandgap [44].

In direct gap materials, both valance band maximum and conduction band minimum have the same  $k$  value. Therefore, if excitation energy is higher than the band gap, electron hole pair is created by excitation of electron to the higher energy states. But for indirect gap materials, conduction band minimum has a  $k$  value different than the valance band maximum. Absorbed photon's wave vector is so small that it cannot change the  $k$  value that much. Hence, phonon has to be absorbed (indicated by a "+" sign) or released (indicated by a "-" sign) for electron to reach the conduction band while the PL process requires the emission of a phonon. The possibility of this process is not that high, meaning that indirect gap materials are generally weak light emitters.

#### **4.6.1 Photon Emission Mechanism**

When electrons are excited to the upper level, they do not remain in that state so long. They immediately relax to the lower energy states within respective bands by emitting phonons. In real semiconductors there are always intentional or unintentional impurities which produce electronic levels inside the band gap. When electron come to the conduction band minimum and hole come to the valance band maximum electron hole pair can recombine radiatively by emitting photons or non-radiatively by emitting energy to some impurities and defects or to a free electron and hole (auger process) in a crystal. Electron-hole pairs can also recombine at surface non-radiatively. Surfaces are strong perturbation of a crystal lattice. There are dangling bonds at the surface because of the breaking of the periodicity. This partially filled electron orbital act as an electronic state at the bandgap, causing non-radiative channel to the carrier [45]. Figure 4.8 shows the relaxation possibilities for an electron in a crystal.

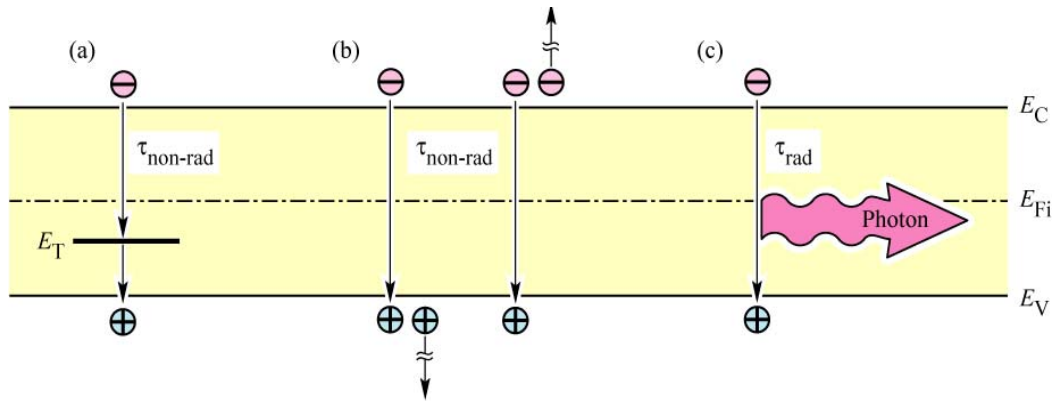


Figure 4.8: Band diagram illustrating non-radiative recombination a) via a deep level, b) via an Auger process (the energy is dissipated by the excitation of a free electron in the conduction band or hole in the valance band) and c) radiative recombination [45].

## CHAPTER 5

### ANALYSIS OF SAMPLES PRODUCED BY E-BEAM EVAPORATION TECHNIQUE

#### 5.1 Sample Preparation

In this work, substrates were p-type Si (100) wafers with resistivity 1-10  $\Omega\text{cm}$ . Different sets of samples were produced to understand light emission from Si nanocrystals and Tb related structures. Both material content and production technique were varied to probe various aspects of this material system. Silicon monoxide (SiO) source was used in the first set of samples prepared by e-beam evaporation, while SiO<sub>2</sub> and Tb sources were used in the second set prepared by magnetron sputtering. The details of the fabrication are given in Table 5.1 and figure 5.1.

Table 5.1: Properties of samples produced by e-beam evaporation technique.

Sample	Base Pressure (Torr)	Layers	Thickness (nm)
S1	$1.7 \times 10^{-6}$	SiO	100
S2	$1.6 \times 10^{-6}$	Si+Tb	175
S3	$1.8 \times 10^{-6}$	SiO <sub>2</sub> +Tb	175
S4	$1.7 \times 10^{-6}$	SiO+Tb	175

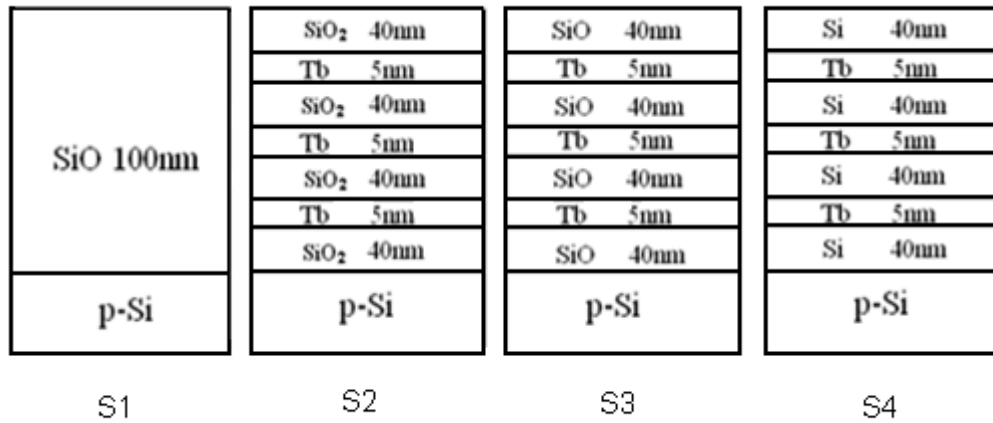


Figure 5.1: Schematics of the produced samples.

Samples were annealed under N<sub>2</sub> and vacuum conditions for different durations and temperatures to see the effect of annealing on luminescence from the silicon nanostructures and Tb<sup>3+</sup> ion.

## 5.2 Characterization

Characterization is an important part of the study to understand different properties of the samples. In this part of the thesis, results of XRD and PL analysis are presented. XRD technique was used to have an idea about new crystalline phases present in the film because different bonding structures between atoms can change the luminescent behavior of the sample. PL technique was employed to see the emission from Si nanocrystals and Tb<sup>3+</sup> ion.

### 5.2.1 X-Ray Diffraction Technique

XRD measurements were performed at a scan speed of the 0.4°/min with the scan step of 0.02° and fixed grazing angle of 0.5°. Figure 5.2 shows the XRD pattern of pure Tb which is taken as the reference data for other samples. Typical Tb peaks

corresponding to (100), (002), (101), (110) and (200) planes are seen in this figure.

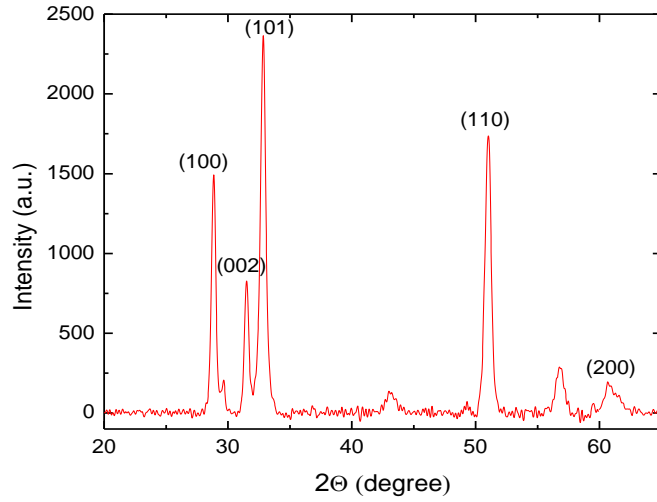


Figure 5.2: XRD spectrum of pure Tb.

The following figure shows the XRD spectra of the samples listed in table 5.1. These samples were annealed under vacuum condition at 1000°C for 30min.

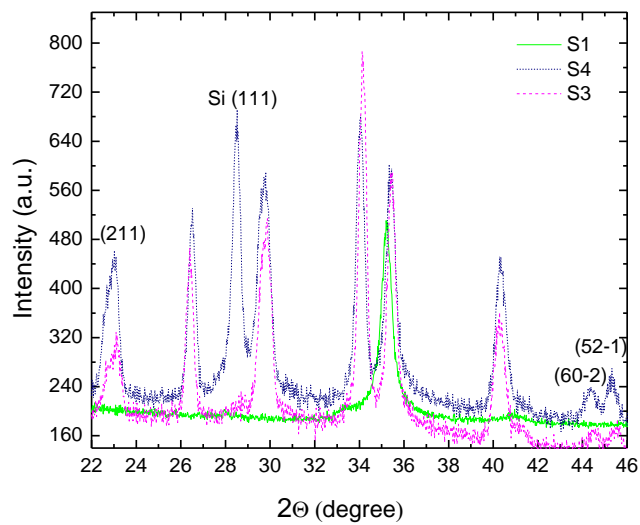


Figure 5.3: XRD spectra of the samples S1, S3 and S4.

After XRD analysis, it was determined that peaks seen in figure 5.3 except  $2\Theta = 23.05^\circ$  [ $\text{Tb}_2\text{SiO}_5$  (2,1,1)],  $2\Theta = 28.52^\circ$  [Si (1,1,1)],  $2\Theta = 34.08^\circ$  [ $\text{Tb}_x\text{O}_y$ ],  $2\Theta = 40.30^\circ$  [ $\text{Tb}_x\text{O}_y$ ],  $2\Theta = 44.54^\circ$  [ $\text{Tb}_2\text{SiO}_5$  (6,0,-2)],  $2\Theta = 45.53^\circ$  [ $\text{Tb}_2\text{SiO}_5$  (5,2,-1)], are related with the  $\text{Tb}_x\text{Si}_y$  compounds. S1 does not have any Tb related peak because of the absence of Tb. This makes sure that  $2\Theta = 35.51^\circ$  peak is not related with the Tb. Although S4 does not contain any intentionally incorporated oxygen in it, Tb-O compound related peak appears in the spectrum. It was shown by Berning G. L. P. that Tb atom is very reactive to oxygen atoms, and oxidation occurs during the annealing process even if there is a capping layer of Si [46]. It was observed that the vacuum level was improved with an order of magnitude during the evaporation. This is showing that Tb atoms are getting oxygen atoms from the evaporation chamber and oxidized. Therefore, Tb-O compound peaks appearing in the XRD spectrum are not surprising. Energy dispersive X-ray spectroscopy (EDS) analysis of the sample also shows that sample contains about 7% oxygen.

It is generally accepted that peak around  $2\Theta = 28.5^\circ$  is coming from the Si (111) crystal planes [47]. Si (111) peak is clearly seen for the S4 and also appears for S2 and S3. Shape of the peak determines the crystallite sizes. Smaller nanocrystals generate broader peaks which can be fitted to Sherrer's formula, while larger ones approaching bulk phase generate sharper XRD peaks. Based on this fact it can be inferred from Figure 5.3 that Si (111) peak is coming from smaller nanocrystals for S3 while S4 with smaller FWHM has larger crystallites as expected from the process parameters. Figure 5.4 shows the closer look at that Si (111) peak region for S2. It is surprising that one can identify two peaks in Si signal. This might be a result of different stress conditions at different position inside the film.

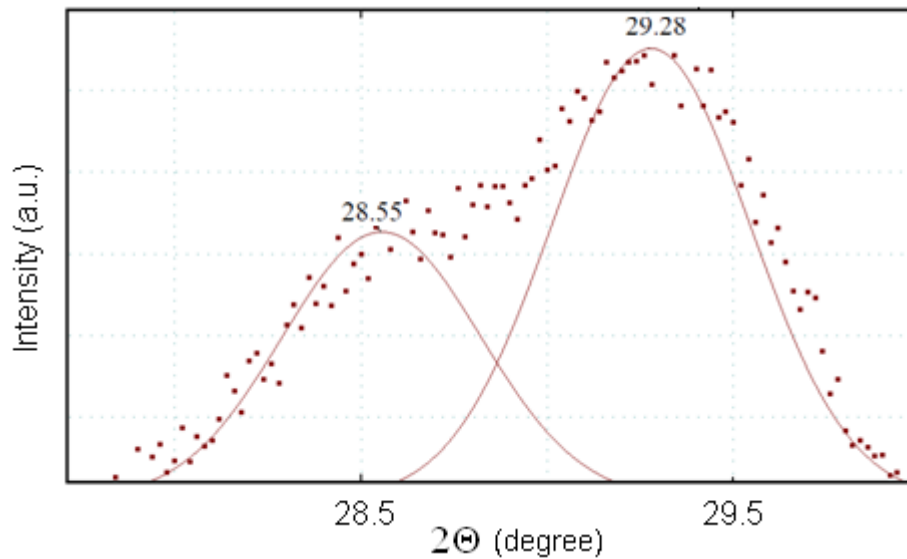


Figure 5.4: XRD peak fit around  $2\theta = 28.5^\circ$  region of S2.

XRD spectrums show that prepared samples containing Tb have 3 different crystal structure formations mainly  $Tb_xO_y$ ,  $Tb_xSi_y$  and  $Tb_xSi_yO_z$ . Relative ratios can differ with the concentration changes and annealing parameters. XRD gives strong evidence of terbium silicide, terbium silicate and terbium oxide formation as mentioned also in previous studies [46, 48].

### 5.2.2 Photoluminescence Spectroscopy

PL technique is very powerful and non-destructive technique to understand the optical properties of the samples. Up to now, many studies were reported on the luminescence from Si nanocrystals and  $Tb^{3+}$  ion emission centers [23, 49-51].

PL experiments were carried out at room temperature with an excitation source of 532nm Nd-YAG and 325nm He-Cd lasers, MS-257 monochromator and Hamamatsu CCD camera. Figure 5.5 shows the PL spectra of the sample S1 without Tb.

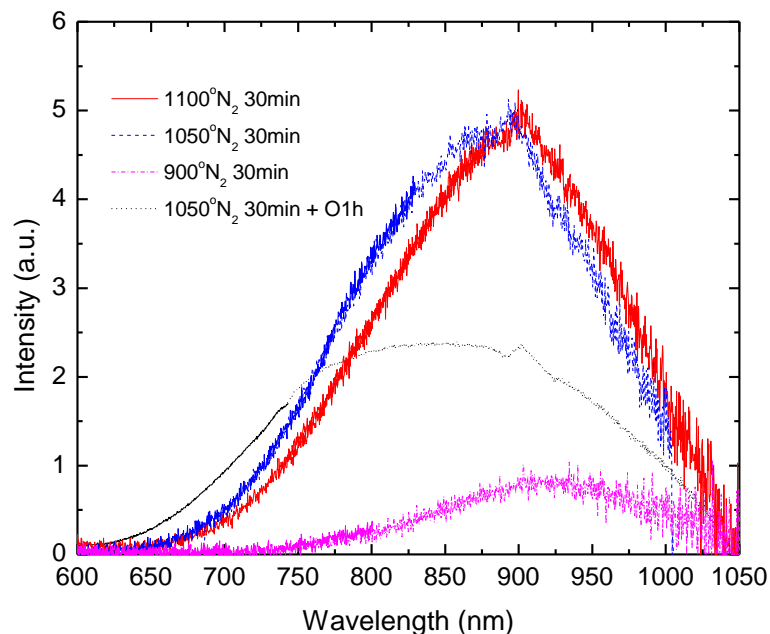


Figure 5.5: Room temperature PL spectrum of S1 excited by Nd-YAG laser.

The emission band between 700-1000 nm for N<sub>2</sub> annealed sample is typically attributed to the recombination in Si nanocrystal [51]. Peak position is depends on the size of the crystal. Higher annealing temperatures yield larger nanocrystals which results increase in the emission wavelength as seen in figure 5.5. When sample was annealed under oxygen, nanocrystal size shrinks due to the SiO<sub>x</sub> formation on the outer shells and blue shift appears. Broadening of the spectrum is related to the Si-O interface state involvements to the luminescence. Although nanocrystal related PL was observed for N<sub>2</sub> annealed sample, it was not for vacuum annealed sample. It is an expected result due to having no Si (111) peak appears in XRD spectrum (figure 5.3).

When He-Cd laser was used as an excitation source, intensity of the PL is increased as seen in the figure 5.6. Increasing the excitation energy increases the intensity of the emission at 750 nm, originated from the small nanocrystallites in a matrix. Note that interference pattern was appeared in the PL spectrum due to the

interference effect of the filter. Although it was eliminated for some samples in this work by using Gaussian fit (figures 5.6-5.7), it remains as it is for the samples which fitting disturbs the general appearance of the PL spectrum.

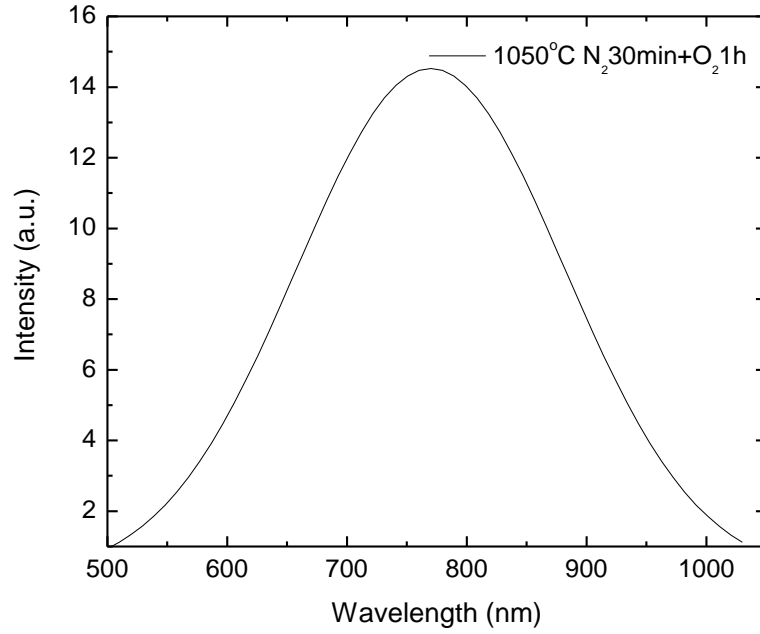


Figure 5.6: Room temperature PL spectrum of S1 annealed at 1050°C under N<sub>2</sub> for 30min then 1050 °C under O<sub>2</sub> for 1h. This spectrum was taken using He-Cd laser operating at 325 nm.

For the second set of samples having Tb inside, He-Cd laser was used for PL excitation. Nd-YAG laser operating at 532 nm did not generate any Tb<sup>3+</sup> ion PL signal as it appears to have a smaller energy than required for optical excitation. Figure 5.7 shows the PL spectrum of the samples. No Tb<sup>3+</sup> ion related PL was observed in S4 possibly due to clustering of Tb<sup>3+</sup> ions while Si crystallites were growing, as detected by XRD. Therefore, PL graph is not displayed here for that sample. For samples S2 and S3, emission from Tb<sup>3+</sup> ion atomic transitions was detected.

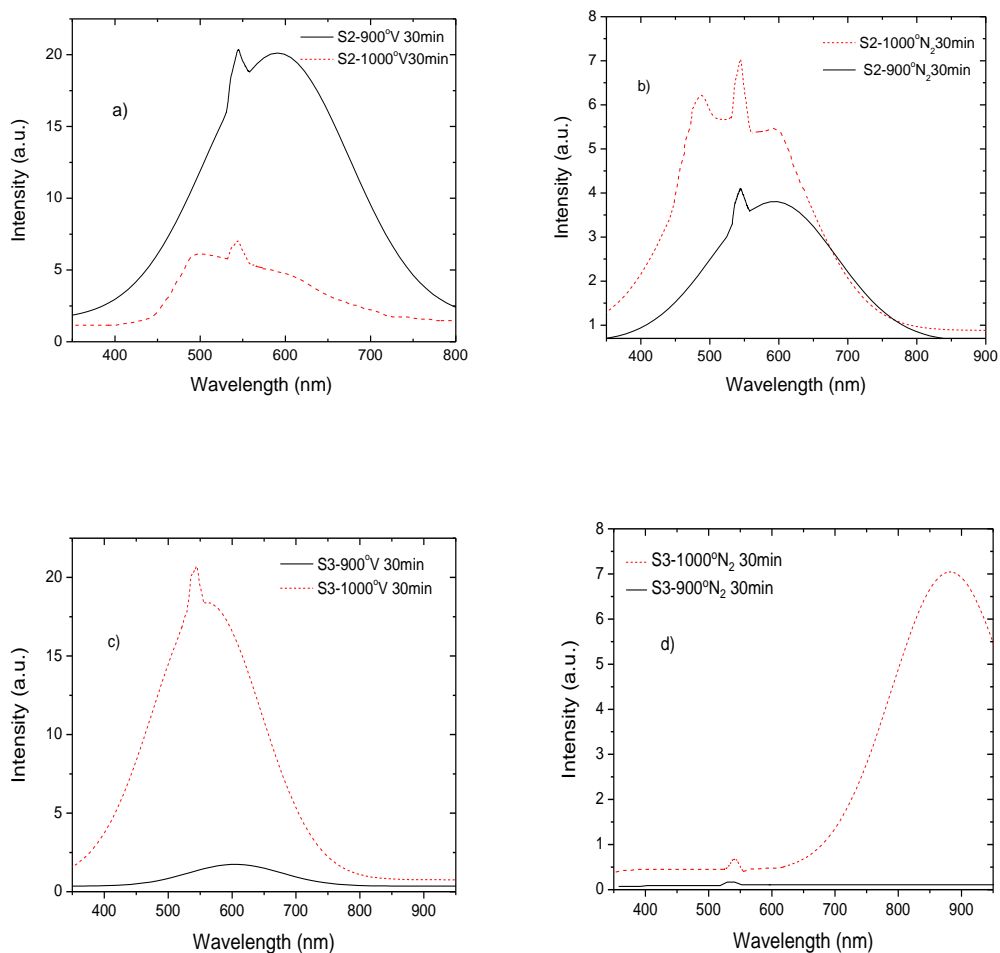


Figure 5.7: PL spectrums of S2 (a,b) and S3 (c,d) annealed under vacuum (a,c) and  $N_2$  (b,d) environments.

As can be seen from figure 5.7a and 5.7b, S2 has two different PL centers. PL at 650nm is due to the commonly known NBOHC defect of  $SiO_2$  matrix. Increasing annealing temperature suppresses NBOHC emission. The peaks seen at 543 nm and at 490 nm are due to the atomic transitions of  $Tb^{3+}$  ion from  $^5D_4$  to the  $^7F_6$  level and from  $^5D_4$  to the  $^7F_5$  level respectively (see Figure 3.1). The peak intensity increases with annealing temperature in both annealing conditions. For the  $N_2$  annealing case, the relative intensity of the NBOHC defect peak is lower with respect to the  $Tb^{3+}$  ion peak seen at 543 nm. This is indicating that NBOHC defects were passivated by the oxygen atoms available in the  $N_2$  ambient. S3 has

lower oxygen concentration than S2, which results NBOHC emission to decrease. Surprisingly, annealing under N<sub>2</sub> at 1000°C yields new peak formation at 890 nm. This peak is believed to be originated from the Si nanocrystals in the matrix. For this sample, both Si nanocrystal peak and Tb<sup>3+</sup> ion atomic transition (from <sup>5</sup>D<sub>4</sub> to the <sup>7</sup>F<sub>6</sub> level) peak appear simultaneously in the spectrum. Therefore, no relation could be found at this stage about energy transfer between Si nanocrystals and Tb<sup>3+</sup> ions. Even though other atomic transitions are expected to appear in the spectrums, due to the broad defect luminescence and filter used, they cannot be detected for both of the samples. Possible excitation mechanism of RE ions in these types of O rich Si matrices will be discussed in Chapter 6 together with the samples produced by sputtering method.

## CHAPTER 6

### ANALYSIS OF SAMPLES PRODUCED BY SPUTTERING TECHNIQUE

#### 6.1 Sample Preparation

In this part of the work, p-type Si (100) substrates were used with resistivity 1-10  $\Omega\text{cm}$ . In order to study the matrix effect on  $\text{Tb}^{3+}$  ion luminescence, 3 types of matrices were studied, namely Si rich  $\text{SiO}_2$ ,  $\text{SiO}_2$  and Si. Table 6.1 summarizes the sample and process parameters used during the fabrication. Figure 6.1 shows schematics of the produced samples.

Table 6.1: Properties of the samples produced by sputtering technique.

Sample	Base Pressure (Torr)	Layers	Tb Pieces	DC Power (Watt)	RF Power (Watt)	Thickness (nm)
Si7	$2.1 \times 10^{-6}$	Si+ $\text{SiO}_2$	0	130	350	50
Si8	$2.1 \times 10^{-6}$	Si+ $\text{SiO}_2$	0	115	350	50
Si9	$2.1 \times 10^{-6}$	Si+ $\text{SiO}_2$	0	100	350	50
Tb1	$2.1 \times 10^{-6}$	Si+ $\text{SiO}_2$ +Tb	4	150	350	100
Tb2	$2.1 \times 10^{-6}$	Si+ $\text{SiO}_2$ +Tb	3	150	350	100
Tb6	$2.0 \times 10^{-6}$	Si+Tb	4	150	0	100
Tb7	$2.1 \times 10^{-6}$	Si+ $\text{SiO}_2$ +Tb	4	150	175	120
Tb8	$2.0 \times 10^{-6}$	$\text{SiO}_2$ +Tb	2	0	175	40

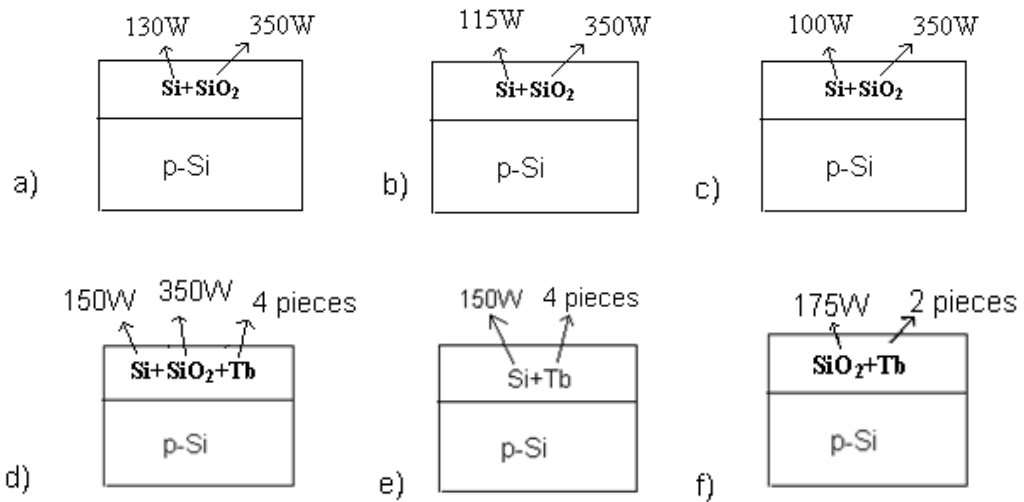


Figure 6.1: Schematics of the sputtered samples. a, b and c represents Si7, Si8, Si9; d, e and f represents Tb1, Tb6, Tb8 respectively.

In order to incorporate Tb atoms into the sputtered film, Tb pieces were put on 3 inch Si, and SiO<sub>2</sub> targets positioned on magnetrons. Each Tb piece roughly had a diameter of 0.5cm so that Si and SiO<sub>2</sub> can also be sputtered with Tb. DC sputtering technique was used for Si while RF sputtering was employed for SiO<sub>2</sub> to avoid charging. For each of the processes electronic grade (6.0) Argon gas was used with  $4 \times 10^{-3}$  Torr pressure during the deposition and 20 sccm flow.

After the deposition, samples were annealed under N<sub>2</sub> and vacuum conditions for different durations and temperatures.

## 6.2 Characterization

Fabricated samples were characterized by XPS, XRD, SEM and PL. XPS was used to study the elemental composition and chemical formations as function of the depth of the grown film. XRD data provided information about the structural formation and also some evidence on the chemical formation in the film. SEM was used to see the surface morphology of the films and EDS analysis provided

compositional information about the samples. Finally, PL technique was employed to see the emission from Si nanocrystals and  $Tb^{3+}$  ions.

### 6.2.1 X-Ray Photoelectron Spectroscopy

XPS measurements were done by an energy step of 0.1 eV in a UHV condition. The background correction and peak fitting was done by using XPSPEAK95 software. XPS signals from the electrons ejected from  $Tb3d_{5/2}$ ,  $Tb3d_{3/2}$ ,  $Si2p_{3/2}$ ,  $O1s$ ,  $C1s$  states were obtained for a set of samples. Depth profile analysis was done only for sample Tb7. Figures 6.2-6.4 show the XPS depth profile of the Tb7 for peaks  $Si2p_{3/2}$ ,  $O1s$ ,  $C1s$  and  $Tb3d_{5/2}$ .

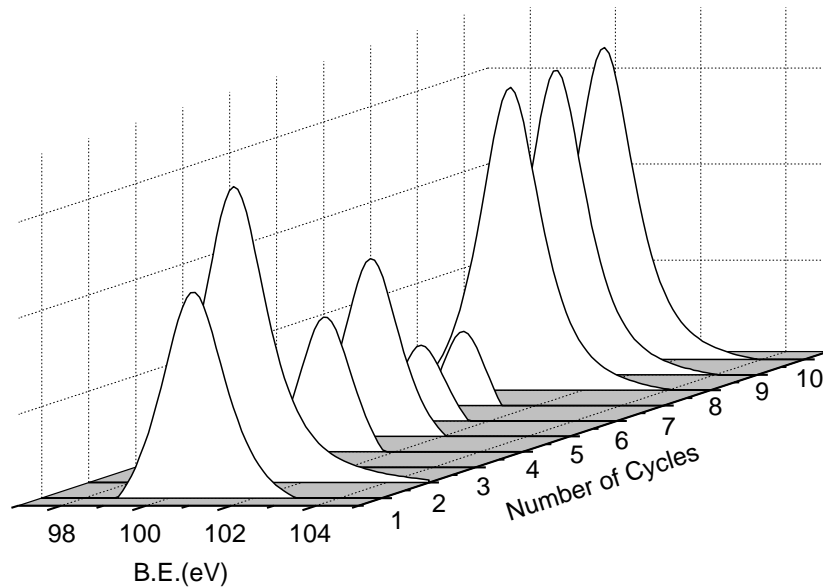


Figure 6.2: XPS depth profile corresponding to the  $Si2p_{3/2}$  state of Tb7 annealed at  $1000^{\circ}C$  for 30min.

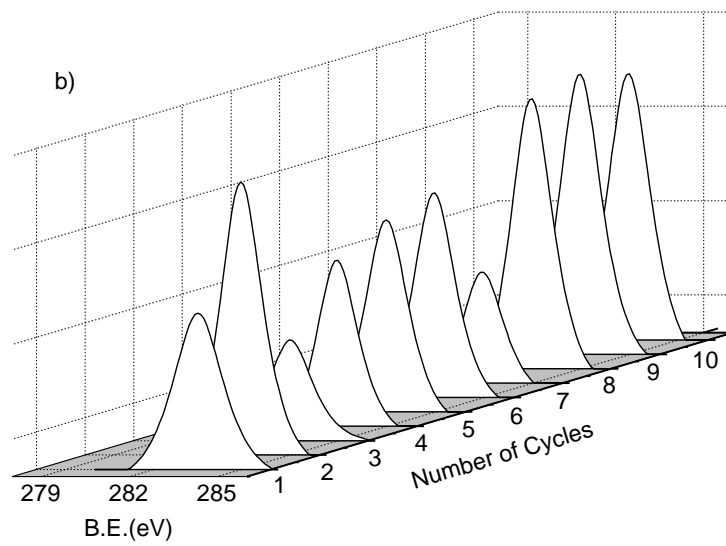
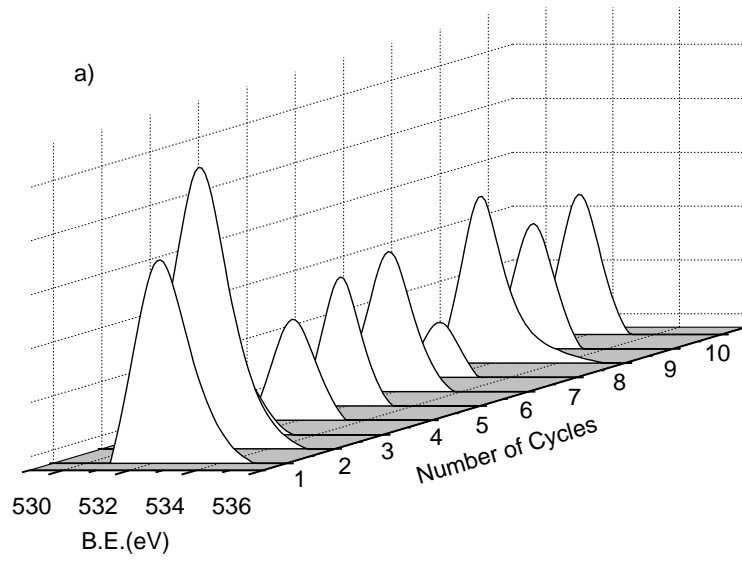


Figure 6.3: XPS depth profiles corresponding to a) O1s and b) C1s states of Tb7 annealed at 1000°C for 30min.

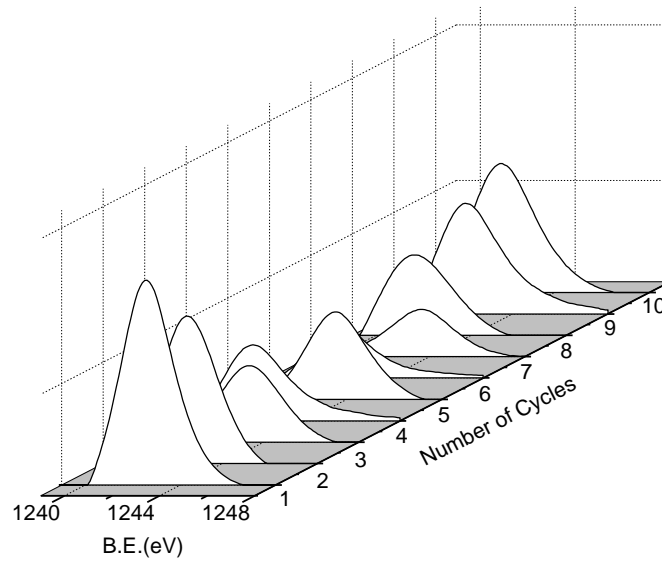


Figure 6.4: XPS depth profile corresponding to the  $Tb3d_{5/2}$  state of Tb7 annealed at  $1000^{\circ}C$  for 30min.

As in the case of e-beam evaporated samples, although no oxygen peak was expected for sample Tb6, O1s peak appears in the XPS spectrum. This is due the oxygen gettinger during Tb sputtering as described above. It seems to be difficult to fabricate oxygen free Tb films under high vacuum conditions. In addition, carbon (C) concentration is higher than the expected amount due to the interaction of the sample with the environment.

Variation of XPS peaks relative to each other was analyzed by using XPS depth profile data. Figure 6.5 and 6.6 show the change of intensity of the main peaks and peak position versus number of sputter cycles, respectively. It is seen in figure 6.5 that variation of Si-C and Tb-O concentration change exhibits almost the same behavior as a function of sputtering cycle. This can be an evidence of  $Si_xC_y$  and  $Tb_xO_y$  formations inside the film.

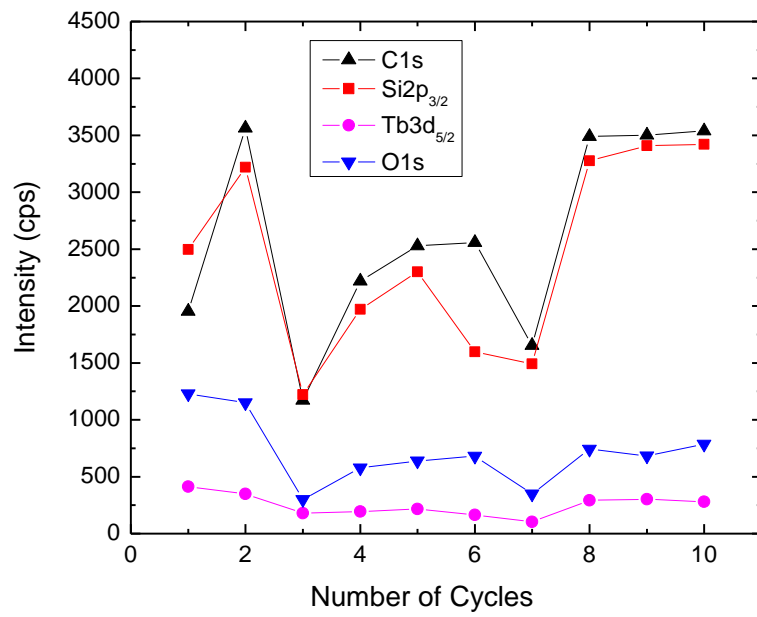
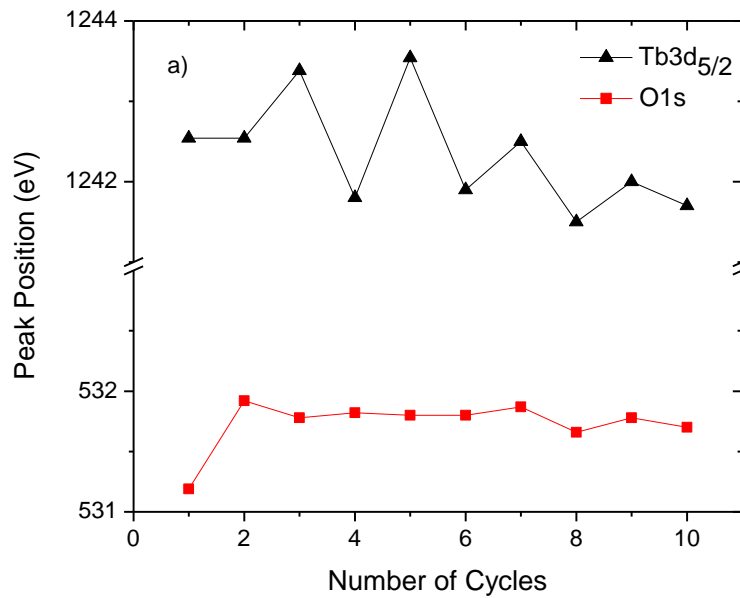


Figure 6.5: The change of intensity of the peaks in each sputter cycle.



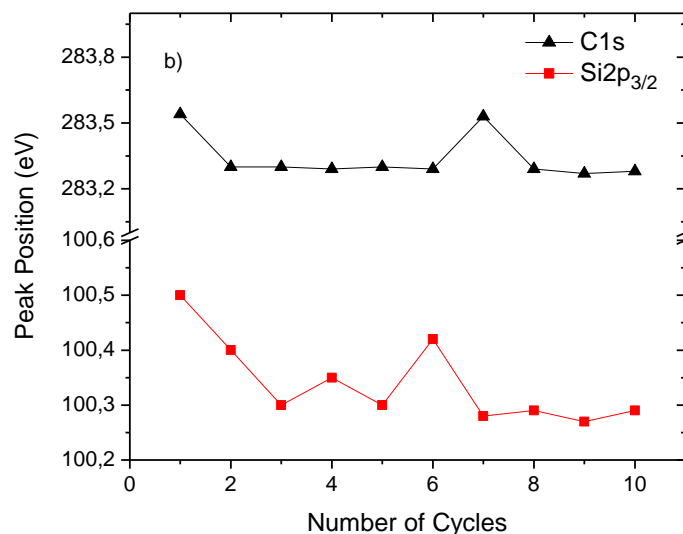


Figure 6.6: Change of XPS peak position corresponding to a) Tb3d<sub>5/2</sub>, O1s b) C1s, Si2p<sub>3/2</sub> states of Tb7 annealed at 1000°C for 30min.

Si2p and C1s XPS peak positions are known to be at 99.2 eV and 284.6 eV respectively. Figure 6.6 shows that for sample Tb7 these peaks appears at 100.3-100.5 eV for Si2p and 283.3-283.5 eV for C1s. These peaks best fit to the peaks of SiC at 100.4 eV and 283.3 eV [51]. Therefore, together with the concentration variation data, it can be concluded that SiC formation occurs in the sample. However, C incorporation was not intentional in any of these samples.

O1s XPS peak position is known to be at 531.8 eV. Figure 6.6 shows that this peak appears at its exact position 531.8 eV except the surface. No shift was detected related to the SiO<sub>2</sub> formation.

Tb3d<sub>5/2</sub> XPS peak position is known to be at 1242 eV. Figure 6.6 shows that this peak changes its position during sputtering. For sputter number 3, 5 and 7 it appears at about 1243.4 eV which is probably related to Si-Tb compounds. For all other cycles except 1 and 2, peak positions change in between 1241.5-1241.8 eV. This peak position region best fits to the Tb<sub>2</sub>O<sub>3</sub> and TbO<sub>2</sub> compound's peak positions at 1241.5 eV [52]. Peak shifts from that value to the higher energy side

can be an evidence of higher oxidation states and may be presence of Tb-Si compounds in the film. Possible higher oxidation state peaks occur for sputter numbers 1 and 2 due to the strong interaction of the top of the sample with the ambient.

## 6.2.2 X-Ray Diffraction

In this part, samples having Tb were studied to understand the correlation between luminescent and structural properties. XRD measurements were performed at a scan speed of the  $0.4^\circ/\text{min}$  with the scan step of  $0.02^\circ$  and fixed grazing angle of  $0.5^\circ$ .

Figure 6.7 shows the XRD spectrum of the samples annealed under vacuum condition at  $1000^\circ\text{C}$  for 30 minutes. The peaks observed are almost at the same positions with the e-beam evaporated samples. Therefore, peaks observed at about  $2\Theta = 23.05^\circ$ ,  $2\Theta = 44.54^\circ$  and  $2\Theta = 45.53^\circ$  are due to scattering from  $\text{Tb}_2\text{SiO}_5$  (2,1,1), (6,0,-2) and (5,2,-1) planes;  $2\Theta = 34.08^\circ$  and  $2\Theta = 40.30^\circ$  are due to scattering from  $\text{Tb}_x\text{O}_y$  and the rest are due to scattering from the  $\text{Tb}_x\text{Si}_y$  compounds.

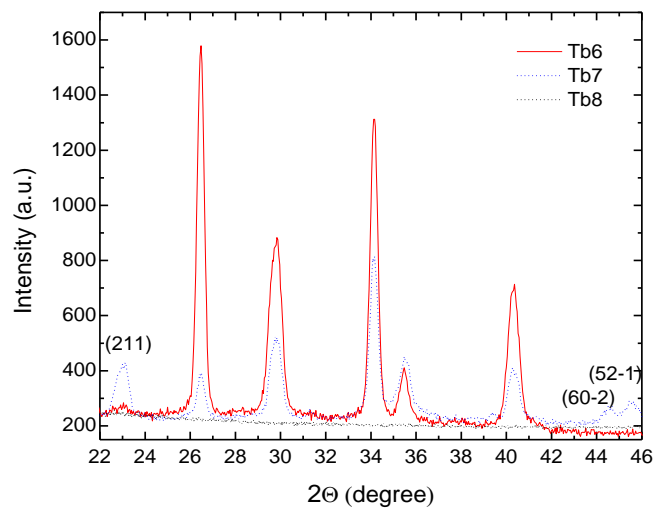


Figure 6.7: XRD spectrum of samples Tb6, Tb7 and Tb8.

As expected from the analysis of the XPS measurements,  $Tb_xO_y$  formation occurs in the samples together with  $Si_xTb_y$  and  $Tb_xSi_yO_z$  compounds. Tb8 shows no feature, probably due to having small amounts of unbounded Si and O atoms that can create Tb-Si-O complexes. Si nanocrystal peak was observed only in the sample Tb1 where amount of Si is expected to be largest (figure 6.8). This peak is quite weak indicating that amount of Si nanocrystal is quite small.

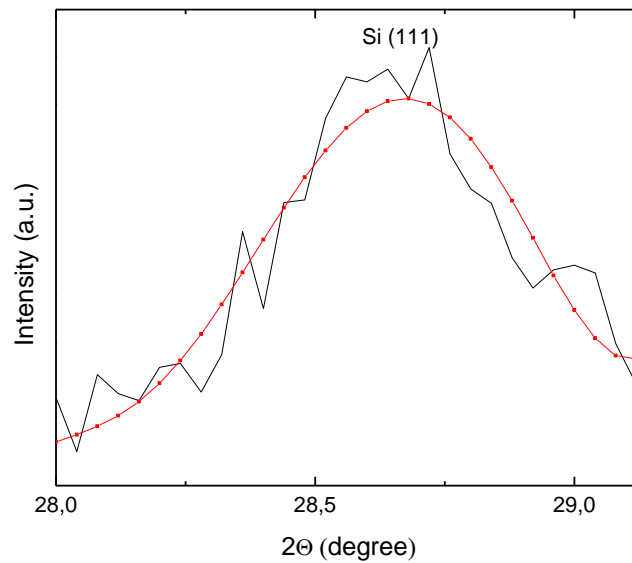


Figure 6.8: Si (111) peak at  $2\theta = 28,6^\circ$  for sample Tb1 annealed at  $1000^\circ\text{C}$  for 30min. under vacuum condition. This peak is known to be originated from Si nanocrystals inside a matrix.

The XRD results are consistent with the study done by the Citrin et al. for Er. Density functional theory calculation studies of him states that Er in O-poor Si matrix prefers to bond Si and generate  $Er_3Si_5$  bonding structure rather than generating point defects [53] due to being energetically more probable. Theory states that this is a result of the allowance of Er-Er metallic bonding. This was also supported by the observation of erbium silicide precipitates by transmission electron microscope in a matrix having very low oxygen concentrations. Being a similar rare earth atom, Tb seems to behave like Er in a similar matrix.

### 6.2.3 Scanning Electron Microscopy

SEM images were taken and EDS analysis were performed to achieve information about the surface and elemental composition of the samples. Figure 6.9 shows the SEM photographs and table 6.2 shows the EDS analysis of the samples with electron energy of 10 keV.

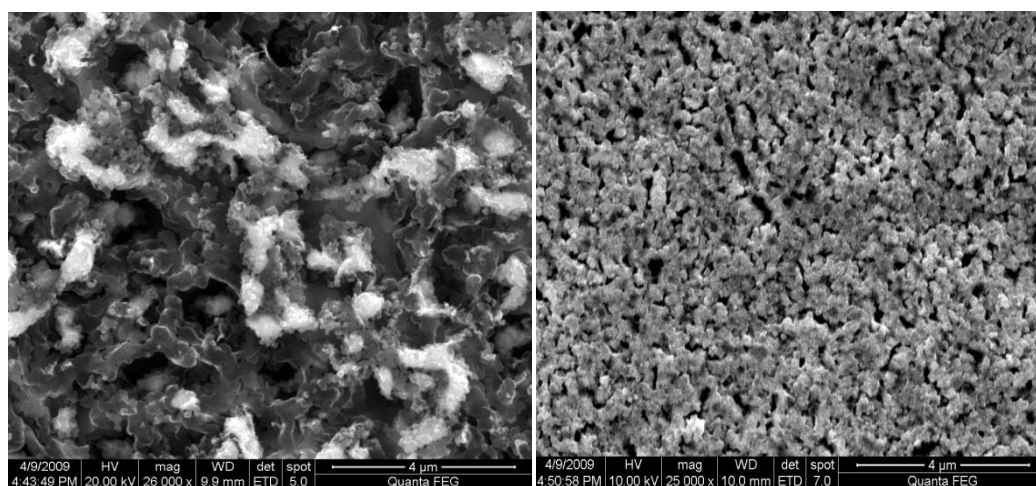


Figure 6.9: SEM photographs of the samples Tb6 (left) and Tb7 (right) annealed at 1000°C for 30min under vacuum condition.

As seen in the SEM photographs surfaces became porous after annealing. Table 6.2 shows the elemental composition of the samples Tb1, Tb6 and Tb7. Tb7-1 and Tb7-2 correspond to different regions of the films.

Table 6.2: Elemental compositions of the samples.

Sample	Si%	O%	Tb%	C%
Tb1 ((N <sub>2</sub> annealed))	31.33	52.4	8.17	8.1
Tb6 (vacuum annealed)	57.22	3.97	1.22	37.59
Tb6 (N <sub>2</sub> annealed)	32.64	50.37	8.79	8.2
Tb7-1 (vacuum annealed)	28.98	29.91	8.61	32.50
Tb7-2 (vacuum annealed)	40.77	4.16	6.57	48.50

There is more than expected C in the samples due to the annealing conditions as mentioned earlier. EDS analysis also confirms the XPS result which suggest that

Tb6 was oxidized during sputtering or annealing. However, C content was found to be much less in the sample annealed in N<sub>2</sub> ambient. Relative concentration of O and Tb in these two regions was found to be important after taking luminescence measurements and will be discussed later.

#### 6.2.4 Photoluminescence Spectroscopy

PL experiments were carried out with excitation sources, 532nm Nd-YAG and 325nm He-Cd lasers at room temperature and temperatures down to 30K. MS-257 monochromator and Hamamatsu CCD camera were used to collect data. Figure 6.10 shows the room temperature PL of samples containing Si rich SiO<sub>2</sub>. Silicon nanocrystal related peak appears in the spectrum like in the samples produced by e-beam technique. When sputter power is increased, Si amount increases in the sample and bigger nanocrystals were formed after annealing. This results in a shift of PL emission through the higher wavelengths as seen in the figure 5.5 and 6.10. Broadening of the PL can be due to the Si-O interface states as mentioned before.

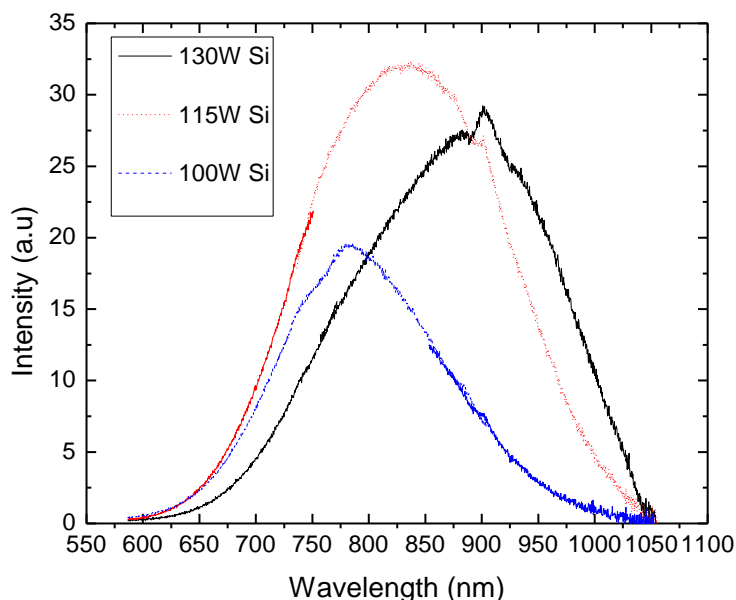


Figure 6.10: PL of Si7, Si8, and Si9 annealed at 1000°C for 3h under N<sub>2</sub> environment. Excitation source was 532nm Nd-YAG laser.

For samples having Tb, only He-Cd laser source was used for excitation due to Nd-YAG laser's smaller energy than required for excitation (figure 6.12). Figure 6.11 shows the PL spectrum of Tb1 which was annealed under N<sub>2</sub> environment for different temperatures and durations to find the optimum annealing condition. It is seen in the figure that even after 700°C annealing, Tb<sup>3+</sup> ion luminescence can be detected around 541nm. Unlike the samples produced by e-beam evaporation, this main Tb<sup>3+</sup> ion peak position is shifted a bit to the lower energy region. This is probably due to the matrix effect on splitting of the energy levels of the RE ion. Annealing at 900°C for 30min generates new emission center at 760nm. This broad emission matches with the generally accepted Si nanocrystal emission band at 700-1000nm. When annealing time was increased at 900°C to 1h, Tb<sup>3+</sup> ion related peak intensity became higher and 760nm peak position did not change while its width broadens. Increasing annealing temperature to 1000°C shows its effects depending on the time of anneal. When sample was annealed for 30min, Tb<sup>3+</sup> ion peak intensity increases while 760nm peak intensity decreases and shifts to the lower wavelength region, which is an unexpected result for nanocrystal emissions. Decrease in the emission intensity of that center with an increase in Tb<sup>3+</sup> ion emission may be an evidence of energy transfer from this emission center to the RE ion. But that explanation seems unreasonable that while room temperature PL spectrum of that center has peak around 1.63 eV (760nm), to excite Tb<sup>3+</sup> ion at least 2.5 eV (488nm) energy is required. Therefore, it appears there are no nanocrystals inside the film and energy transfer does not occur to the RE ion. However, this observed behavior can be explained by two mechanisms: First possible mechanism is that emissions observed may not be due to band to band transition inside the nanocrystal, indeed due to recombination of exciton localized in a trap level inside the bandgap. This can be further evidenced when annealing time was increased to 1h (figure 6.12). In that case, it was only Tb<sup>3+</sup> ion luminescence appearing in the spectrum which can be linked to the mentioned trap levels that there is a decrease in the trap levels by increasing the temperature with an enhancement of the carriers inside the band levels of the nanocrystal, which then excites the RE ion. Same effect was demonstrated by Li J. et al. that although the emission was observed at 800nm, transmission electron microscope

data shows that size of the Si nanocrystals were around 2nm having ~2.7 eV bandgap, which is sufficient for  $Tb^{3+}$  ion excitation [54]. Observing the same effect, it can be stated that there are Si nanocrystals inside Tb1 and energy transfer between Si nanocrystals and  $Tb^{3+}$  ions occurs inside the film enhancing PL intensity of  $Tb^{3+}$  ion. Second possible mechanism explaining the observed behavior is that 760nm peak is due to emission from the nanocrystals in the matrix and the presence of  $Tb^{3+}$  ions in the environment modifies the chemical formation kinetics. In this mechanism it seems that  $Tb^{3+}$  ions react with the already formed Si nanocrystals to form Tb-Si-O complexes. This lead to dissociation of nanocrystals into smaller clusters which has larger bandgap. The blue shift and the intensity reduction in the spectrum are then observed in the PL spectrum. An additional annealing at 1000 °C for 30 min results in total quenching of PL from the Si nanocrystals. Making an analogy with Er-Si system, one can suggest that the relative variation between nanocrystal emission and  $Tb^{3+}$  ion emission is due to the direct energy transfer from Si nanocrystals to  $Tb^{3+}$  ion. But due to having lower emission energy than required for excitation, light emission from  $Tb^{3+}$  ions and its variation with annealing conditions can be described by a model based on Tb-Si-O trap assisted excitation of  $Tb^{3+}$  ions rather than nanocrystals. Trap state related mechanism was explained before for Tb-O compound [see figure 3.4]. The mechanism of excitation is the same while the trap position inside the bandgap changes for these two different trap formations. As a further evidence for trap assisted emission, we see a decrease in the emission intensity when the sample was annealed for a longer time (figure 6.12), which can also be connected to the creation of new trap levels with dissociation of the nanocrystals. In figure 6.11 Gaussian fitting was done for peak at 760nm to eliminate the interference pattern appeared.

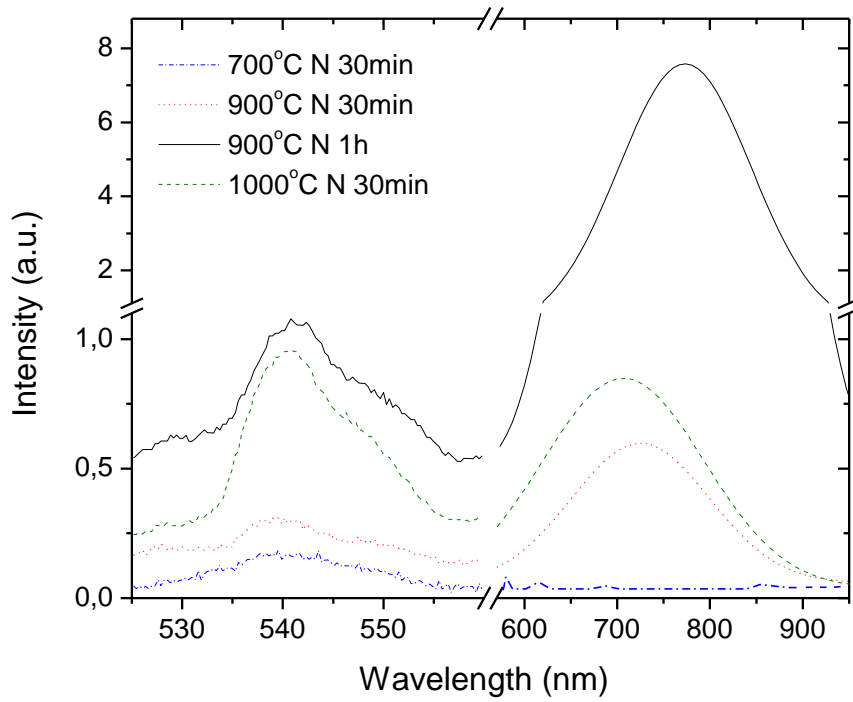


Figure 6.11: PL spectrum of Tb1 annealed at different temperatures and durations.

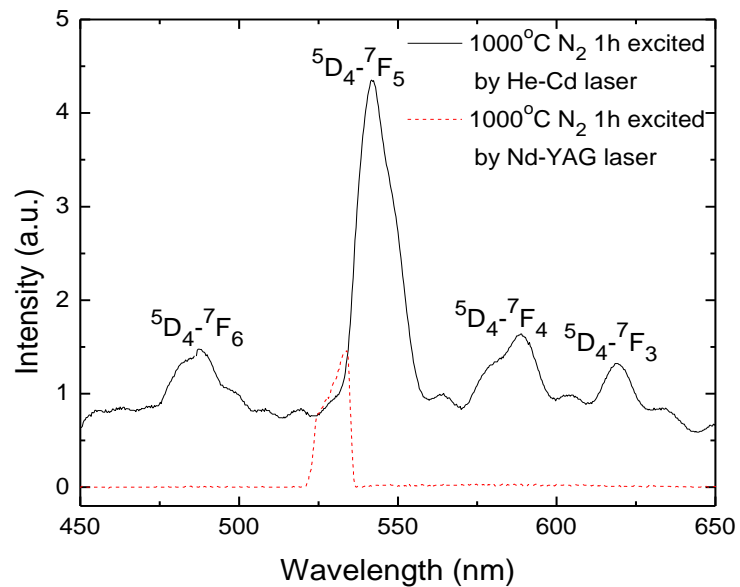


Figure 6.12: Room temperature PL of Tb1 annealed at 1000°C for 1h under N<sub>2</sub> environment excited by He-Cd and Nd-YAG laser.

In this work it was observed that light generation by  $\text{Tb}^{3+}$  ions is very sensitive to the annealing conditions. Figure 6.13 shows the room temperature PL of the Tb1 after vacuum annealing. After  $900^\circ\text{C}$  annealing, oxide defect luminescence shadows the emission from  $\text{Tb}^{3+}$  ion. But annealing at  $1000^\circ\text{C}$  saturates the defect centers and increases the  $\text{Tb}^{3+}$  ion emission. Note that peaks due to the transitions from  $^5\text{D}_3$  level to  $^7\text{F}_j$  ( $j=1-6$ ) levels cannot be seen in the spectrum due to the cross relaxation process as mentioned before.

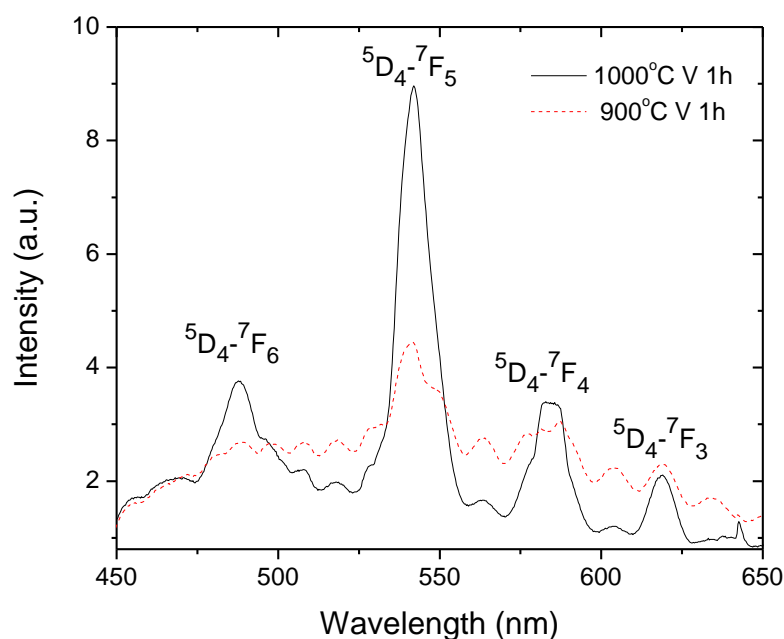


Figure 6.13: PL spectrum of Tb1 annealed at  $900^\circ\text{C}$  and  $1000^\circ\text{C}$  for 1h under vacuum ( $10^{-5}$  Torr) environment.

Upon comparison it was investigated that when samples annealed under vacuum condition yielded stronger PL signal. In general, PL efficiency is much better under vacuum annealing than that of under  $\text{N}_2$  for all samples. This result suggests that during annealing under  $\text{N}_2$  environment  $\text{Tb}^{3+}$  ion is oxidized by trace amount of  $\text{O}_2$  present in the ambient. Although we believe that oxygen plays a role in the formation of trap levels which are active in the luminescence process, excess

oxygen results in further oxidation and thus inactivating the trap states. It is known that Tb is more easily oxidized than Si [48]. Oxidation may result in either less probable cross relaxation process, which restricts the concentration quenching, or formation of shallower trap level so that it loses carriers before exciting the RE ion as mentioned earlier. In addition, for vacuum annealing case  $Tb^{3+}$  ion is known to diffuse through the surface and the substrate [55] which makes ions closer to each other and possibly causing smaller Tb-O complexes which have trap levels suitable for excitation of  $Tb^{3+}$  ion. It should be noted that when annealing temperature increased to  $1100^{\circ}C$   $Tb^{3+}$  ion PL intensity gets smaller for all samples due to clustering of  $Tb^{3+}$  ion which increases the ion-ion interactions by decreasing luminescence lifetime and efficiency.

In order to study the matrix effect on luminescence from  $Tb^{3+}$  ion, samples with different oxygen content were studied. Samples with higher oxygen (Tb8) and lower oxygen (Tb7) than Tb1 in their as form in addition to the sample without any intentional oxygen (Tb6) were identically processed. Results are displayed in figures 6.14-6.16. It is seen from the figures 6.14 and 6.15 that sample Tb8 (without excess Si) exhibits a broad PL peak which is typically observed in  $SiO_x$  films with oxygen deficiency while Tb6 show sharp room temperature PL originated from  $Tb^{3+}$  ion atomic transitions.

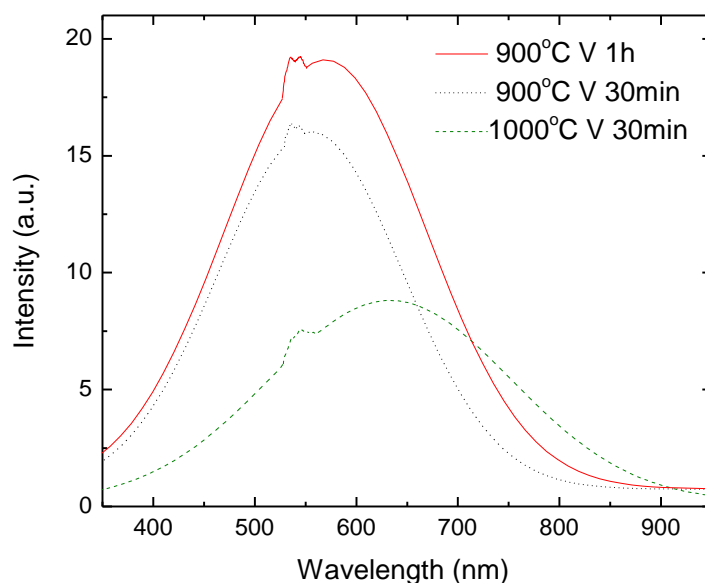


Figure 6.14: PL spectrum of Tb8 annealed under vacuum ( $10^{-5}$  Torr) environment at 900°C and 1000°C for 30min and 1h.

Figure 6.14 shows that sample annealed under 900°C have PL centered about 550nm while sample annealed under 1000°C has PL centered about 650nm. They are both due to the defects in the oxide. Although this broad defect luminescence includes a weak 543nm emission  $Tb^{3+}$  ion atomic transition from  $^5D_4$  to  $^7F_5$  level this signal is too weak to draw certain conclusion. However, it was observed that  $Tb^{3+}$  ion emission is stronger in the oxygen rich sample, showing that  $Tb^{3+}$  ion emission requires the presence of excess Si in the matrix. It can be concluded that  $Tb^{3+}$  ion in a pure silica matrix is not capable of generating light.

Samples Tb6 and Tb7-1 (specific part of the sample Tb7) having excess Si were also annealed under vacuum with the same conditions and drastic increase in the PL intensity was achieved as seen in figures 6.15 and 6.16. Unlike Tb1, stark splitting, splitting of the energy states due to the crystal field, can easily be seen in Tb6 PL spectra (figure 6.15). PL from other side of the Tb7, namely Tb7-2, is not given here due to having very small intensity. The reason for this behavior can be

lower amount of O inside the film (table 6.2) which results in less Tb-O trap levels responsible for the excitation of the RE ion.

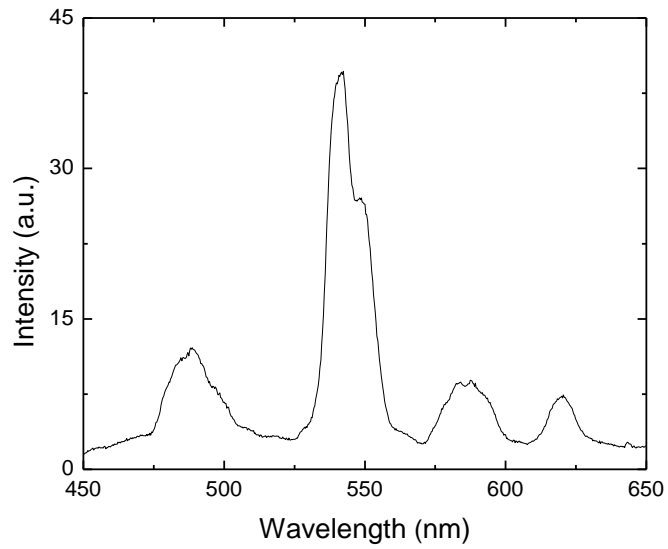


Figure 6.15: Room temperature PL of Tb6 annealed at 1000°C for 30min. under vacuum condition ( $10^{-5}$  Torr).

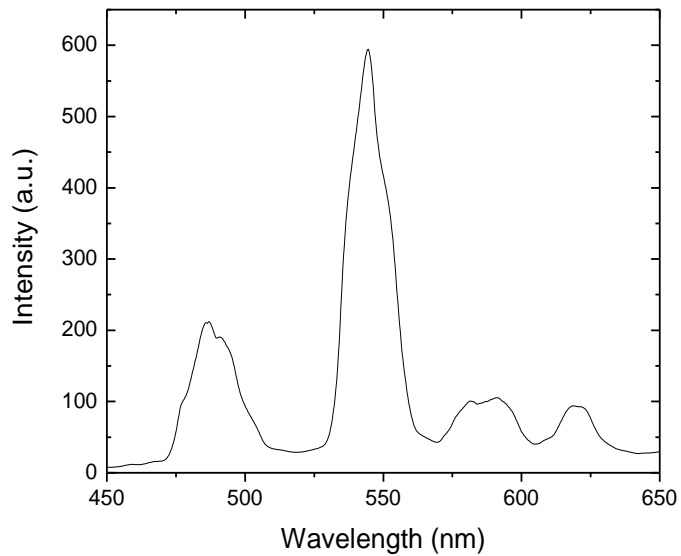


Figure 6.16: Room temperature PL of Tb7-1 annealed at 1000°C for 30min. under vacuum condition ( $10^{-5}$  Torr).

By looking at the intensity scale of emissions for each sample, it is observed that Tb7-1 has emission more than 15 times intense than that of Tb6. The reason for this increment is believed due to three time increase of both O and Tb concentration of the Tb7-1 than Tb6 detected from EDS analysis (table 6.2) in a specific part of the sample. It seems that concentration increase of O with the same amount of increase of Tb in Tb7-1 does not yield higher oxidation states; it rather creates more Tb-O related centers in the film which are known to create trap levels and excite  $Tb^{3+}$  ions. Showing two different PL behaviors with two different O and Tb concentrations is indicative of importance of Tb/O ratio.

In order to understand effect of oxidation on the PL properties, high temperature annealing under oxygen ambient was performed. In this process Tb1 was annealed under  $O_2$  after vacuum annealing, both at  $1000^\circ C$  for 1h. The result is shown in Figure 6.17. It was observed that light emission is totally quenched after oxidation.

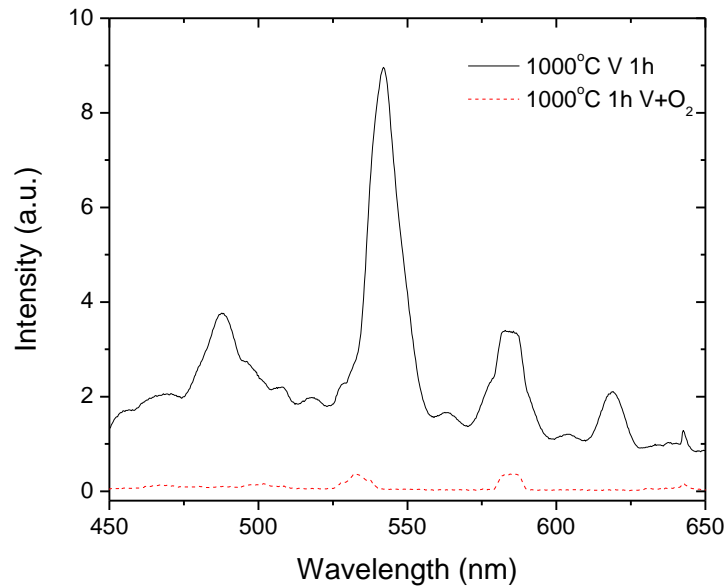


Figure 6.17: Room temperature PL of Tb1 annealed at  $1000^\circ C$  for 1h under vacuum environment and vacuum +  $O_2$  environment. Excitation source was 325nm He-Cd laser.

It can be concluded that light emission from  $Tb^{3+}$  ions embedded into the matrix either requires presence of trap levels in the bandgap or nanocrystals inside the film. All of the luminescence involved levels should be located at a suitable position where both optical absorption and subsequent energy transfer to  $Tb^{3+}$  ions are possible. Trap levels can be created due to  $Tb_2O_3$  or  $TbO_2$  compounds as suggested before. As also evidenced by XRD data, formation of  $Tb_xSi_yO_z$  complexes is correlated with the light emission. It is then reasonable to assume that  $Tb_xSi_yO_z$  structures also create trap states which participates in the light conversion process. We showed that simultaneous emission from Si nanocrystals and Tb is not observable (except for a special case) because these structures do not co-exist chemically.  $Tb^{3+}$  ion reacts with Si at high temperature and with the involvement of oxygen, which is available inside the matrix material, and  $Tb_xSi_yO_z$  is easily formed at the expense of dissociation of Si nanocrystals. Although this mechanism seems to be works well, there may be another mechanism in which nanocrystals transfer energy to excite  $Tb^{3+}$  ions without dissociation, as discussed before. In some cases both trap assisted and nanocrystal assisted excitation mechanisms can exist together. The necessity for energy transfer mechanisms was demonstrated by Zeng X. et al. that, owing to not have resonant optical absorption band at 325nm, if there is no energy transfer to the RE ion, PL could not be obtained by He-Cd laser excitation [56].

These inferences agrees with the results obtained from other works indicating that Si nanoparticles are not required for RE ion to emit light [23] but they enhances the emission by suppressing energy back transfer, reducing temperature quenching [57] and producing energy transfer.

#### **6.2.4.1 Effect of Carbon Implantation on Photoluminescence**

The reason for C implantation was to promote creation of high energy exciton that can excite  $Tb^{3+}$  ion. Enhancement of the  $Tb^{3+}$  ion luminescence was achieved before by using this technique [58]. Figure 6.18 shows the PL of the sample Tb8 after C implantation (40 keV with a dose of  $5.10^{16} \text{ cm}^{-2}$ ) and  $N_2$  annealing.

While the intensity of the defect luminescence did not change after C implantation when compared with vacuum annealed samples,  $Tb^{3+}$  ion luminescence was highly improved. Note that although C implantation was also done for Tb6 and Tb7, no improvement was detected for these samples. It was inferred that C implantation did not create exciton levels; instead it saturates luminescence quenching O-defect centers in O-rich matrix increasing  $Tb^{3+}$  ion luminescence. Due to having smaller amount of oxygen inside, Tb6 and Tb7 does not contain these types of defects that much so that C implantation has no effect on these samples. Note that 428nm peak is due to He-Cd laser and the interference pattern appeared is due to filter used in this experiment. Gaussian fitting did not performed to preserve the peaks appeared.

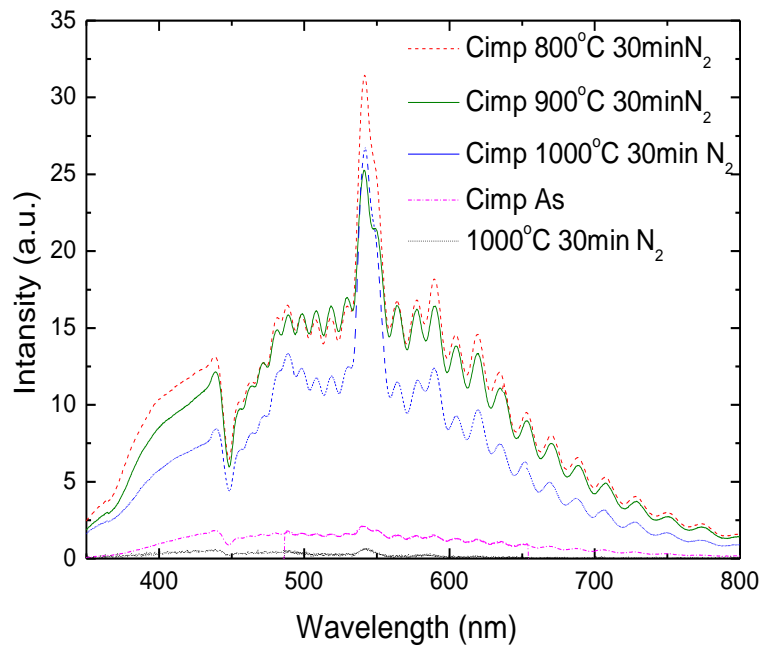
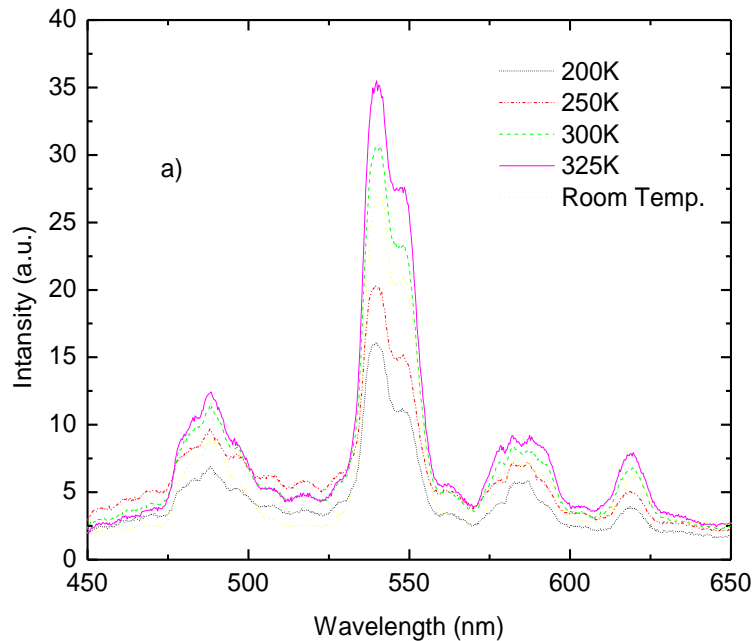


Figure 6.18: PL spectrum of Tb8 annealed under  $N_2$  environment before and after C implantation at 800°C, 900°C, 1000°C for 30min.

#### 6.2.4.2 Temperature Dependent Photoluminescence

Temperature dependence measurements may provide important information about the transitions kinetics. Especially, relative population of different energy levels can be understood from such measurements. Presence of RE trap levels in a matrix can be probed by scanning temperature while taking PL measurement. It is expected that increasing the measurement temperature may lead to loss of electrons localized on a RE trap level. This electron can then make a transition through non-radiative channel, resulting in less luminescence from the sample [59]. In this work, temperature dependent PL experiments were carried out for the samples Tb6 and Tb2. PL data taken at different temperatures are displayed figures 6.19 and 6.20.

The variation of peak intensity as a function of temperature is shown in figure 6.21. We see that, for both samples, PL signal increases significantly at low temperatures. This is in agreement with the reported results on similar samples.



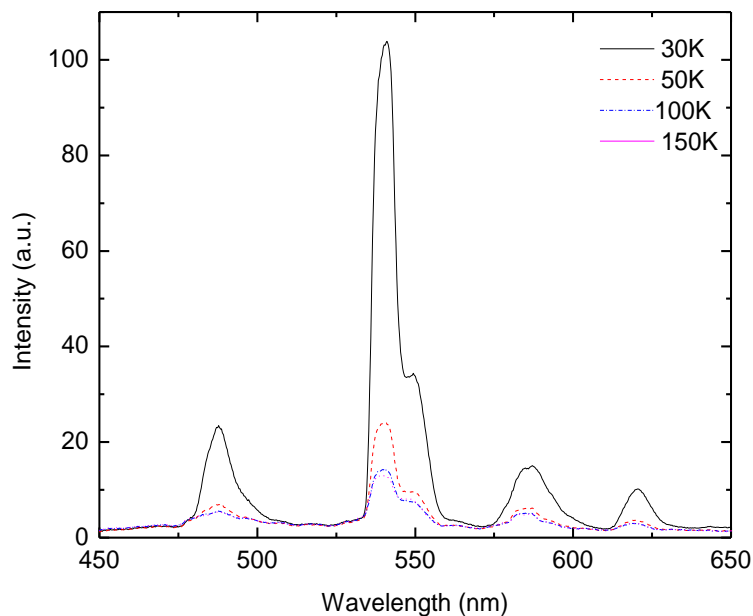
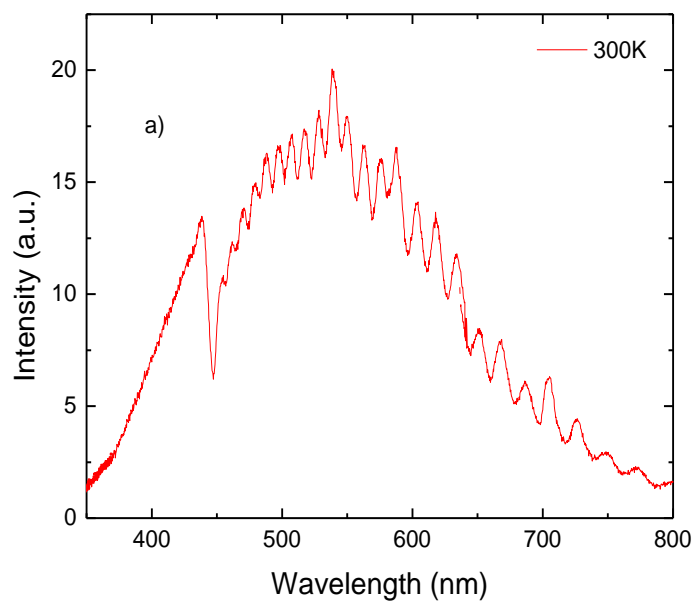


Figure 6.19: Temperature dependent PL spectrum of Tb6 after annealing under vacuum at 1000<sup>0</sup>C for 30min. a) for temperatures higher than 200K b) for temperatures lower than 150K.



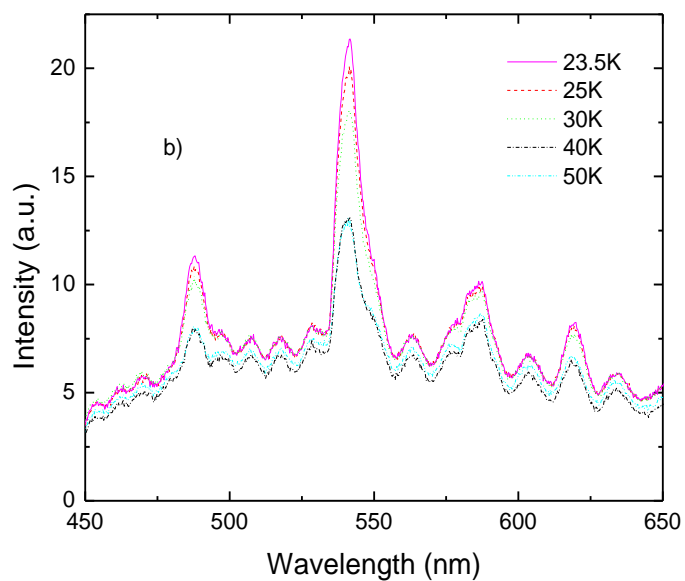


Figure 6.20: Temperature dependent PL spectrum of Tb2 after annealing under vacuum at 1000<sup>0</sup>C for 30min. a) at 300K b) for temperatures lower than 50K. Data taken between temperatures 300-50K was not included in PL spectrums to avoid confusion due to the broad defect luminescence.

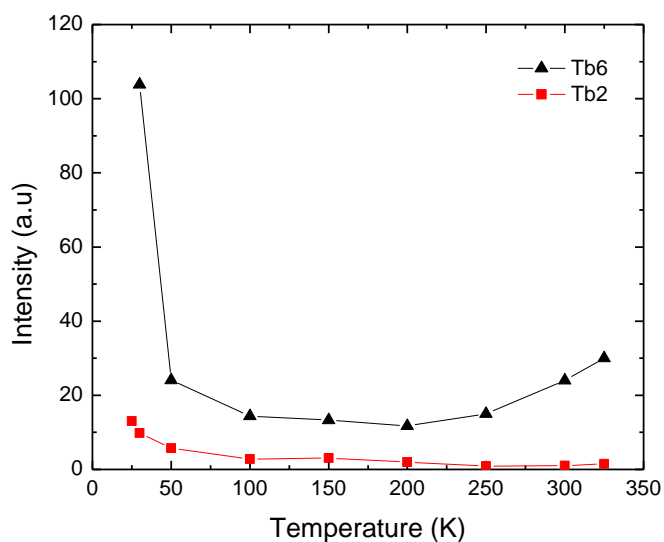


Figure 6.21: Change of PL intensity of Tb6 and Tb2 with respect to change of temperature.

Although general trend of the temperature variation of the emission is similar to the theory stated by Elhouichet et al. [31], the saturation of the intensity could not be observed in our case. There is a strong variation in the luminescence signal between the temperatures 30-50K for Tb6 and also Tb2. For temperatures up to 200K luminescence intensity decreased for both samples. After that level, while PL intensity of Tb2 continues to decrease, there is a slight increase for Tb6 which may be because of involvement of another center, which is active above 250K, to the luminescence of  $Tb^{3+}$  ion. Therefore, it can be inferred that temperature dependence of luminescence of  $Tb^{3+}$  ion in Si based matrices is stronger than that of previously reported matrices such as GaP. This may be due to having Tb related trap levels responsible for excitation nearer to the conduction band in Si based matrices, which can easily ionized even at low temperatures.

## CHAPTER 7

### CONCLUSIONS

In this work, films containing Si nanocrystals and Tb atoms were fabricated by e-beam evaporation and magnetron sputtering techniques. After film growth, samples were annealed at different temperatures and durations to investigate the Si nanocrystal formation and excitation mechanisms of Tb<sup>3+</sup> ion in different matrices. Analyses of the samples were done to have information about the structures and properties of the samples by XRD, XPS, SEM and PL techniques.

It was shown that Si concentration and annealing temperature are key factors affecting nanocrystal formation. Evolution of luminescence properties of nanocrystals was monitored by PL for both production techniques. We observed the expected quantum size effect in the luminescence from nanocrystals: when we increase the annealing temperature the PL peak shifts to larger wavelength due to the decrease in the bandgap. In contrast, annealing under O<sub>2</sub> makes the nanocrystal size smaller resulting in a blue shift in the PL signals.

Although Tb<sup>3+</sup> ion atomic transitions are expected to be independent from the properties of the matrix they are residing due to shielding of the f-shell electrons, excitation process of the ions is strongly depend on the optical properties of the matrix. XRD analysis of samples showed that Tb compounds with Si and O were formed in the films. It is expected these compounds to be either in the form of Tb-O, Si-Tb or Si-O-Tb depending on the concentration of species, annealing temperature or annealing time. In addition,  $2\theta = 28.5^\circ$  peak appeared in the spectrum for some samples is an indication of Si nanocrystal formation. In most of the cases light emission from the nanocrystals could not be detected by PL

spectroscopy. Only in few cases under special experimental conditions we observed PL signal from nanocrystals or probably trap state inside the nanocrystal. The signal was quenched after high temperature annealing either due to the deformation of the nanocrystal by the chemical formation with Tb or due to increase of the carriers in the conduction band of the nanocrystal by a decrease in the trap levels, which then results in transfer of energy to the RE ion. This was seen in the relative variation of PL signal from nanocrystal and  $Tb^{3+}$  ions. It was shown that  $Tb^{3+}$  ion emission is not only related to nanocrystal formation as we have seen strong light emission from the sample where we saw no clue for the presence of nanocrystals. On the other hand, PL can only be obtained in the sample with excess Si. We concluded that light generation takes place via excitation of  $Tb^{3+}$  ion by the absorption of energy via nanocrystals, Tb-Si-O or Tb-O trap level. Even though it seems to be unreasonable for samples without any intentional O incorporation, we observed from XPS that O1s peak appears in these samples. In addition, oxygen containing compounds were detected by XRD. Being aware of the fact that Tb is easily oxidized with a trace amount of O in the environment, we can expect its oxidation in any step of production. This assumption was validated also by the EDS analysis that there is more than expected O appearing in the sample containing only Si and Tb. Although these trap levels are known to excite the  $Tb^{3+}$  ion, depending on the number of oxygen bond, trap level may become shallower and easily loose the carrier without exciting  $Tb^{3+}$  ion. This was to happen by detecting the extinction of the  $Tb^{3+}$  ion related luminescence from the PL spectrum of the sample after oxidation process.

Temperature dependence of the PL spectrum was studied and it was observed that PL peak intensity increases at low temperature. This is in agreement with the commonly observed behavior. However, transition temperature from low intensity to the high intensity is lower than previously published results. This indicates that  $Tb^{3+}$  ion have closer trap levels to the conduction band inside the silica based matrix compared to reported data obtained from GaP matrix. Shallow trap state enables carriers to be excited to the conduction band easily instead of making radiative transition. An interesting feature we observed in the temperature dependent measurements was the slight increase of PL intensity after 250K for

Tb6. This increase maybe because of other possible excitation channel activating at higher temperatures.

It was shown in this study that fully stoichiometric SiO<sub>2</sub> matrix does not yield an efficient Tb<sup>3+</sup> ion luminescence. In order to obtain a measurable Tb<sup>3+</sup> ion emission, the host matrix should contain less oxygen (i.e, excess Si). From the analysis of various spectroscopic data, we concluded that the intensity of the PL is enhanced when relative concentration of Tb and O is in the 1:3-4 interval, with Tb concentration not below than 1%. Although further study is needed to establish more precise data, this result is an important outcome towards achieving efficient RE luminescence in Si based matrices.

This work is very important that it brighten the way of RE based Si light emitters by studying all different approaches in one hand and having important inferences for all the possible paths of emission. As a further study on this subject, role of SiC formed in a matrix can be analyzed and by controlling the relative amounts of the atoms inside the film and creating optimal annealing conditions, light emitting diode structure can be produced and studied in details.

This work has attempted to fabricate and understand the light emitting materials based on Si nanostructures with and without Tb inclusion. It has been demonstrated that light emission through different transitions of Tb<sup>3+</sup> ions are possible in silica matrix having excess Si. The light generation mechanism is a function of complicated chemical structures formed by Tb, Si and O. It was evidenced that Tb-Si-O and Tb-O compounds creates a trap state in the Si rich silica matrix, which provides an energy transfer. Incoming photons are absorbed by these states and/or Si nanostructures depending on the process conditions and transfer the absorbed energy to excite Tb<sup>3+</sup> ions for light emission. Effect of other phase formations such as SiC in the silica matrix has also been studied to some extent. Effective light generation has been obtained by forming SiC structure with ion implantation. However, C involvement needs to be studied further to obtain conclusive results.

## REFERENCES

- [1] Micron; About Semiconductors: History,  
<http://www.micron.com/k12/semiconductors/history>, 2009.
- [2] Kenyon, A. J.; *Semiconductor Science and Technology*, 20, 65 (2005).
- [3] Berning G. L. P., Swart H.C., Roos W.D.; *Applied Surface Science*, 73, 305 (1993).
- [4] Rodriguez, A., Misra M., Hesselbom H., Tove P. A.; *Solid-State Electronics*, 19, 17 (1976).
- [5] Canham, L. T.; *Appl. Phys. Lett.*, 57, 1046, (1990).
- [6] Dobkin D. M.; *Silicon Dioxide: Properties and Applications*,  
<http://www.enigmatic-consulting.com>, 2009.
- [7] University of Tasmania; *Covalent Network Substances*,  
<http://www.utas.edu.au>, 2009.
- [8] Pacchioni G., Skuja L., Griskom D. L.; *Defects in SiO<sub>2</sub> and Related Dielectrics: Science and Technology*; p. 94-109.
- [9] Skuja L.; *Journal of Non-Crystalline Solids*, 239, 16, (1998).
- [10] Trukhin A. N., Jansons J., Fitting H. J., Barfels T., Schmidt B.; *Journal of Non-Crystalline Solids*, 331, 91, (2003).
- [11] Gaponenko S. V.; *Optical Properties of Semiconductor Nanocrystals*, p.65 (1998).
- [12] Irrera A.; *Light Emitting Devices Based on Silicon Nanostructures*, PhD Thesis.
- [13] Walters R. J.; *Silicon Nanocrystals For Silicon Photonics*, PhD Thesis, May 2007.

- [14] Delerue C., Allan G., Lannoo M.; *Journal of Luminescence*, 80, 65, (1999).
- [15] Kovalev D.; *Phys. Stat. Sol. (b)*, 215, 871 (1999).
- [16] Ostwald W.; *Lehrbuch der Allgemeinen Chemie*, vol. 2, part 1. Leipzig, Germany (1896).
- [17] Kulakci M.; *Silicon Nanocrystals Embedded in Silicon Dioxide for Light Emitting Diode Applications*, Ms Thesis (2005).
- [18] Pavesi L.; *Photonics*, 6125, 12508 (2006).
- [19] Castagna M. E., Coffa S., Monaco M., Muscara A., Caristia M., Lorenti S., Messina A.; *Material Science and Engineering B*, 105, 83 (2003).
- [20] Helm M., Sun J., Potfajova J., Dekorsy T., Schmidt B., Skorupa W. ; *Microelectronics Journal*, 36, 957 (2005).
- [21] Sun J.M., Skorupa W., Dekorsy T., Helm M.; *J. of Appl. Phys.*, 97, 123513 (2005).
- [22] Han K.H., Park M. B., Cho N. H.; *Surface Science*, 514, 117 (2002).
- [23] Gao W., Li T., Ono Y., Hsu S. T.; *Journal of Rare Earths*; 24, 673 (2006).
- [24] Diecke G. H.; *Spectra and energy levels of rare earth ions in crystals*, New York : Wiley-Interscience (1968).
- [25] Ortis C. P.; *Spectroscopy of Terbium Doped Sol-gel Glasses*, Thesis (2007).
- [26] Wang S., Amekure H., Eckau A., Carius R., Buchal Ch.; *Nuclear Instruments and Methods in Physics Research B*, 148, 481 (1999).
- [27] Yassievich I. N., Kimerling L. C.; *Semicond Sci. Technol.*; 8, 718, (1993).
- [28] Evans-Freeman J. H., Peaker A. R.; *Silicon Based Materials and Devices*, Volume 2, 247 (2001).
- [29] Jones R.; *Optical materials*, 28, 718 (2006).
- [30] Needles M., Schlüter M., and Lannoo M.; *Phys. Rev. B*, 47, 15533 (1993).

- [31] Coffa S., Priolo F., Franzo G., Bellanu V., Carnera A., and Spinella C.; Phys. Rev. B, 48, 11782 (1993).
- [32] Elhouichet H., Oueslati M., Lorrain N., Langa S., Tiginyanu I. M., Föll H.; Phys. Stat. Sol. (a), 202, 1513 (2005).
- [33] Coffa S., Priolo F., Franzo G., Bellani V., Carnera A., Spinella C.; Phys. Rev. B, 48, 16 (1993).
- [34] Kenyon A. J.; *Progress in Quantum Electronics*, 26, 225 (2002).
- [35] AJA International, INC.; What is Sputtering, <http://www.ajaint.com/whatis.htm>, 2009.
- [36] Dogan I.; *Fabrication and Characterization of Alumina and Silicon/Alumina Films with Silicon Nanocrystals Formed by Magnetron Co-Sputtering Technique*, Ms Thesis (2008).
- [37] Slovak Academy of Sciences; Physical Vapor Deposition, <http://www.umms.sav.sk/index.php?ID=415>, 2009.
- [38] Michigan University; Lecture Notes, <http://www.cem.msu.edu/~cem924sg/LectureNotes.html>, 2009.
- [39] Wagner C. D., Riggs W. M., Davis L. E., Moulder J. F., Muilenberg G. E.; *Handbook of X-Ray Photoelectron Spectroscopy*. Pelkin-Elmer Corporation, Minnesota, 1978.
- [40] U.S. Department of Interior; X-ray Diffraction Primer, <http://pubs.usgs.gov/of/2001/of01-041/htmldocs/xrpd.htm>, 2009.
- [41] P. Scherrer, *Gottinger Nachrichten*, 2, 98, 1918
- [42] Central Laboratory; X-ray Diffractometer, <http://www.centrallab.metu.edu.tr>, 2009.
- [43] Sproul W. D., Christie D. J., Carter D. C.; *Thin Solid Films*, 491, 1 (2005).

- [44] Caltech University; Excitation of Photoluminescence,  
<http://nedwww.ipac.caltech.edu/level5/Sept03/Li/Li4.html>, 2009.
- [45] Schubert E. F.; *Light Emitting Diodes*, Cambridge (2003).
- [46] Berning G. L. P., Theron C. C., Swart H. C.; *Applied Surface Science*, 157, 129 (2000).
- [47] Yerci S., Serincan U., Dogan I., Tokay S., Genisel M., Aydinli A.; *J. of Appl. Phys.*, 100, 074301 (2006).
- [48] Berning G.L.P., Swart H. C., Witt B.; *Applied Surface Science*, 64, 1 (1993).
- [49] Ferraioli L., Wang M., Pucker G., Navarro-Urrios D., Daldosso N., Kompocholis C., Pavesi L.; *Journal of Nanomaterials*, 43491 (2007).
- [50] Kahler U., Hofmeister H.; *Optical Materials*, 17, 83 (2001).
- [51] Kulakçı M., Serincan U., Turan R.; *Semicond. Sci. Technol.*, 21,1527 (2006).
- [52] <http://techdb.podzone.net/xpsstate-e/index.cgi?element=O>
- [53] Citrin P. H., Hamann D. R., Northrup P. A.; *Physica B*, 308, 369 (2001).
- [54] Li J., Zalloum H.Y., Heng C. L., Wojcik C., Mascher P.; *Advances in Optical Technologies*, 295601 (2008).
- [55] Berning G. L. P., Sward H. C.; *Surface and Interface Analysis*, 26, 420 (1998).
- [56] Zeng X., Yuan J., Zhang L., *J. Phys. C.*; 112, 3503 (2008).
- [57] Yuan F. C., Ran G. Z., Chen Y., Dai L., Qiao Y. P., Ma Z. C., Zong W. H., Qin G. G.; *Thin Solid Films*, 409, 194 (2002).
- [58] Seo Y., Shin J. H.; *Appl. Phys. Lett.*, 84, 22 (2004).
- [59] Elhouichet H., Oueslati M.; *Phys. Stat. Sol. (a)*, 204, 1497 (2007).